SUPPORTING INFORMATION FOR

Significant variability in photocatalytic activity of natural titanium-containing minerals: implications for understanding and predicting atmospheric mineral dust photochemistry

Maya Abou-Ghanem,[1] Anton O. Oliynyk,[1,2] Zhihao Chen,[1] Laura C. Matchett,[1], Devon T. McGrath,[3] Michael J. Katz,[3] Andrew J. Locock,[4] and Sarah A. Styler[1,5]*

* corresponding author.
Email: stylers@mcmaster.ca

[1] Department of Chemistry, University of Alberta, Edmonton, Alberta, Canada T6G 2G2
[2] Chemistry and Biochemistry Department, Manhattan College, Riverdale, New York, USA 10471
[3] Department of Chemistry, Memorial University of Newfoundland, St. John's, Newfoundland and Labrador, Canada A1C 5S7
[4] Department of Earth and Atmospheric Sciences, University of Alberta, Edmonton, Alberta, Canada T6G 2G2
[5] Department of Chemistry and Chemical Biology, McMaster University, Hamilton, Ontario, Canada L8S 4L8

Number of figures: 14
Number of tables: 20
Number of pages: 70

1 Experimental details and sample characterization

2 Supporting results and discussion

3 References

4 Supporting figures

5 Supporting tables

S5–14	Electron microprobe data for natural minerals
S15	XRD table for Pawley fit for minerals
S16–20	XRD tables for single crystal diffraction

1 Experimental details and sample characterization

1.1 Photochemical coated-wall flow tube reactor

All experiments were conducted in a newly constructed photochemical coated-wall flow tube reactor system under ambient temperature and pressure conditions. A schematic of the system is provided in **Figure S1** and the parameters of the flow tube are shown in **Table S1**.

The flow tube itself is constructed of Pyrex 7740 (34.4 cm length, 1.6 cm id, 0.7 cm thickness water jacket). Insert tubes, also constructed from Pyrex 7740 (20.0 cm length, 1.05 cm id), were coated with the mineral sample of interest and placed inside the flow tube. Mounted in the center of a black plastic box, the flow tube is surrounded by four Sylvania 25W BL UV-A lamps (300–410 nm, λ_{max}: 356 nm). To verify that the light intensity inside the flow tube was atmospherically relevant, the photolysis frequency of NO_2 (J_{NO_2}) was investigated and found to be 0.0045 ± 0.0001 s^{-1} (see **Section 1.2**), which is in the range of the photolysis rate constants found in the atmosphere[1,2].

The temperature inside the reactor was controlled by a recirculating chiller (RTE-140, Neslab), which was set to 296.5 K. To avoid any microbial growth inside the chiller that could potentially absorb UV radiation in the water jacket layer, the common biocide chloramine-T was added to the chiller water. The chiller water was frequently monitored to verify that its absorbance spectrum in the UV-A range matched that of deionized water.

Dry, purified zero air for experiments was produced using a commercial zero air generator (747-30 reactor type A, Aadco Instruments). Ozone was generated in the dry air flow using

a commercial ozone generator (97-0066-01, UVP) and monitored at the exit of the flow tube using a photometric ozone analyzer (T400, Teledyne). Acquisition of the ozone data was accomplished by connecting the ozone analyzer to an analog-to-digital converter (U6, LabJack) and collecting the data using a custom-built LabVIEW program at 5 s intervals.

The flow tube system contains 4 mass flow controllers (MFCs; MC-2SLPM-D/5M, Alicat), 3 of which were used to control the flows of ozone in dry air, dry air, and wet air prior to the flow tube. The flow of dry air through the ozone generator was held constant at 100 sccm, and the relative humidity (RH) in the flow tube was varied by changing the flow ratio between the dry and wet MFCs. Wet air was generated by passing dry air through a water bubbler. RH in the system was monitored by 3 in-line humidity/temperature sensors (SHT75, Sensirion), which were placed directly after the zero air generator in order to make sure the zero air was dry (RH reading of 0.1%), prior to the flow tube, and at the exit of the flow tube; RH values prior to and at the exit of the flow tube were always ± 1% of the values reported in our figures and text. A customized Arduino was employed to convert RH analog signals into a digital output that was collected using a custom-built LabVIEW program at 5 s intervals.

The total flow upstream of the flow tube was set equal to 400 sccm for all experiments. Since the ozone analyzer requires a flow rate of 750 sccm, a fourth MFC was placed at the outlet of the flow tube to add an additional mass flow of 500 sccm, with excess flow directed to exhaust; all reported ozone concentrations were corrected for this dilution.

When experiments were not being conducted, the coated-wall flow tube reactor was continuously flushed with zero air (400 sccm); in addition, the RH of the zero air flow was

adjusted as described above at the end of each day to reflect the desired RH for the subsequent day's experiments.

1.2 Determination of NO_2 photolysis frequency (J_{NO_2}) for the flow tube reactor

Irradiance inside the flow tube was quantified using NO_2 actinometry[1,2], in which the magnitude of production of NO from NO_2 upon illumination is used to determine the photolysis frequency for NO_2, J_{NO_2}.

In these experiments, which were conducted at ambient temperature and pressure, NO_2 (4.93 ppm ± 5% in N_2, Certified Standard, Praxair) was diluted with N_2 (5.0 grade, Praxair) upstream of the flow tube to lead to a final concentration of ~370 ppb. A Na_2CO_3 denuder was placed upstream of the flow tube to remove any HONO formed in the cylinder regulator or wetted parts of the MFCs. The denuder consisted of a sandblasted Pyrex tube (37.5 cm length, 0.635 cm outer diameter), the interior surface of which was coated with Na_2CO_3 solution previously prepared by adding 1 g of glycerol and 1 g of Na_2CO_3 to 50 mL of methanol. The coating solution was dripped into the Pyrex tube, which was then dried with N_2 (5.0 grade, Praxair) prior to use.

Upon illumination, the increase in NO and decrease in NO_2 were measured using a chemiluminescence NO_x (NO + NO_2) analyzer (T200U, Teledyne). To prevent the photolysis of NO_2 in undesired areas and control the illuminated volume inside the flow tube, all but 8.5 cm of the length of the flow tube was covered with aluminum foil; in order to ensure the light intensity within the reactor was identical to that in our dust photochemistry

experiments, these experiments were conducted with a Pyrex insert tube placed inside the flow tube. From these data, J_{NO_2} was obtained as follows[2]:

$$[NO_2]_{avg} = [NO_2]_{final} + \frac{1}{2}\Delta[NO]$$

$$J_{NO_2} = \frac{\Delta[NO]}{[NO_2]_{avg}} \times \frac{F}{V} \times \frac{1}{\phi} \times \frac{1}{T}$$

Here, $[NO_2]_{final}$ is the concentration of NO_2 at the exit of the illuminated flow tube, $\Delta[NO]$ is the increase in NO concentration upon illumination, F is the volumetric flow rate in L s^{-1}, V is the illuminated volume of the reactor in L, ϕ represents the quantum yield of NO production, and T represents the transmission factor of the lamps through the reactor walls.

The quantum yield of NO from the photolysis of NO_2 in N_2 depends on several subsequent reactions induced by the formation of NO. Using the principal reactions described in Zafonte et al.[2], we derive a quantum yield of 1.63 for NO for our experimental conditions, which is in good agreement with the values reported by these authors. Finally, we note that we set the value of T as unity, because we are interested in measuring the irradiance within the flow tube rather than the inherent emission profile of the lamps.

Experimental protocol for J_{NO_2} determination involved first establishing a steady concentration of NO_2 in the dark (~360 ppb) followed by the following illumination protocol: 20 min light (1 lamp), 20 min dark, 20 min light (2 lamps), 20 min dark, 20 min light (3 lamps), 20 min dark, 20 min light (4 lamps), and 20 min dark. This procedure was conducted in triplicate, with results shown in **Figure S2.** A maximum photolysis frequency

173 of 0.0045 ± 0.0001 s^{-1} was obtained for NO_2 when all 4 lamps were turned on inside the
174 reactor, which is similar to the photolysis frequency of NO_2 in the atmosphere and indicates
175 an atmospherically relevant irradiance inside the flow tube[1,2].

176 **1.3 Experimental details**

177 **1.3.1 Pyrex insert tube preparation**

178 Pyrex insert tubes were cleaned prior to use by first placing each tube in a 1% H_2SO_4 bath
179 for 1 min followed by a concentrated base bath for 1 h. After the base bath, the tubes were
180 thoroughly rinsed with deionized water and dried in a gravity oven (100L, Fisherbrand™)
181 at 324 ± 5 K.

182 The acid bath was prepared by adding 10 mL of concentrated H_2SO_4 to 990 mL of deionized
183 water. The base bath was prepared by adding 1 L of 2-propanol to 166 mL of deionized
184 water, followed by adding 41.7 g of solid KOH pellets and mixing until fully dissolved.

185 **1.3.1.1 Tube coating procedure for natural minerals**

186 Each coated tube was prepared by adding ~50 mg of Ti-containing mineral to a Pyrex
187 insert tube, followed by several drops of deionized water to form a slurry. The tube was
188 then stoppered with rubber stoppers (No. 00), rotated until the slurry covered the entire
189 inner surface of the tube, and placed on a hot dog roller (RHD800 Retro Series Hot Dog
190 Roller, Nostalgia Electrics) at maximum temperature to allow the mineral sample to dry in
191 an even layer. After drying, the first 5 cm of one end of the tube and the first 1 cm of the
192 other end were wiped clean using moistened laboratory wipes (Kimberly-Clark

193 Professional™). The first 5 cm was wiped to allow the ozone-containing gas flow to achieve
194 laminar flow prior to its interaction with the mineral surface (see **Table S1**); the last 1 cm
195 was wiped due to the formation of an uneven coating at the tube ends from the use of the
196 stoppers. The coated tubes were placed in a gravity oven (100L, Fisherbrand™) at 324 ± 5
197 K overnight prior to use.

198 The mass of mineral inside each Pyrex insert tube was determined by weighing by
199 difference on an analytical balance (AB265-S/FACT, Mettler Toledo). Coated tubes were
200 weighed after each experiment; then, they were rinsed with a tap water/Sparkleen™
201 mixture, distilled water, methanol, and deionized water, placed in a gravity oven (100L,
202 Fisherbrand™) at 324 ± 5 K overnight to dry, and weighed again.

203 **1.3.1.2 Tube coating procedure for TiO_2 minerals (commercial and natural)**

204 For both the commercial and natural TiO_2 samples, almost complete depletion of ozone was
205 observed upon illumination, which resulted in a diffusion correction of several orders of
206 magnitude for γ (as discussed in main text of the manuscript). Mixing of TiO_2 with
207 photochemically inert SiO_2 has been previously been used to mitigate the effect of
208 significant depletion of ozone from the gas-phase reservoir upon exposure to illuminated
209 TiO_2[3]; in this study, a similar strategy was employed.

210 TiO_2/SiO_2 mixed films were prepared by first sonicating SiO_2 in 30 mL of deionized water
211 for 1 h (2.8 L Ultrasonic Bath, Fisher Scientific) to reduce the agglomeration of SiO_2 in the
212 coating procedure, then transferring TiO_2 powder to the SiO_2 suspension. To ensure
213 quantitative TiO_2 transfer, 1 mL of water was used to rinse the weighing tray that

214 contained the TiO_2. The resultant mixture was stirred with a PTFE stir bar (1 inch,
215 Fisherbrand™) to ensure homogeneous mixing of TiO_2 and SiO_2 particles; after 10 min, 1
216 mL was pipetted into a Pyrex insert tube and the same coating procedure described in
217 **Section 1.3.1.1** was applied. Because each TiO_2 sample type displayed significantly
218 different reactivity, different TiO_2 loadings were employed for each TiO_2 sample; the
219 masses of both TiO_2 and SiO_2 used for each sample type are shown in **Table S2**.

220 **1.3.2 Experimental protocol**

221 At the beginning of each experiment, a Pyrex insert tube coated with the mineral substrate
222 of interest was placed in the coated-wall flow tube reactor, the movable injector was
223 retracted, and the coating was exposed for 30 min to zero air at the experimental RH. Then,
224 the injector was pushed in past the mineral coating, preventing exposure of the sample to
225 the gas flow, and the ozone generator was turned on. After 45 min, at which point a stable
226 ozone concentration was achieved, the injector was pulled back and samples were exposed
227 to ozone. After 1 h of dark exposure, samples were illuminated for 1 h; after an additional
228 30 min of dark exposure, the injector was again pushed in in order to verify that there was
229 no drift in ozone concentrations throughout the experiment; after 30 min, the ozone
230 generator was turned off and ozone concentrations were recorded for an additional 5 min.
231 The average ozone concentrations over the last 5 min in the light, dark, and with the
232 injector pushed in were used in the calculations described in main text of the manuscript.

233 Experiments were performed in triplicate for all minerals at 25% RH; selected reaction
234 profiles for each mineral sample are shown in **Figures S3–4**. For some minerals,

experiments were also performed as a function of RH (here, experiments were only performed once at each RH value); representative reaction profiles are shown in **Figure S5**.

1.3.3 Considerations in calculations of uptake coefficients

In this work, we quantify the reactivity of ozone with Ti-containing minerals using a quantity known as an uptake coefficient (γ)[4], which is defined as the number of ozone molecules taken up by the surface divided by the total number of collisions of ozone molecules with the surface. Previous studies of trace gas–dust interactions have reported both initial[5–7] and steady-state[5,7–9] uptake coefficients; because the latter is most relevant for the behavior of dust over extended timescales in the atmosphere, we report it here.

In our system, laminar flow conditions (Reynolds number < 2000) and continuum flow regimes (Knudsen number << 1) are applicable (see **Table S1)**; therefore, at high values of γ, where significant depletion of ozone occurs near the sample surface, γ_{eff} can be limited by the diffusion of ozone from the centre of the flow tube to the sample surface. In order to correct for underestimations in γ_{eff} as a result of these radial diffusion limitations, a correction factor is applied using the CKD method[10] as described in the main text of the manuscript. We note that we chose mineral sample masses such that reported uptake coefficients had a maximum correction for radial diffusion of 30% from γ_{eff}:

1.3.3.1 Additional considerations for TiO_2 samples

As described in **Section 1.3.1.2**, in order to minimize the need for excessive corrections for gas-phase diffusion limitations, we employed TiO_2/SiO_2 mixed films for all TiO_2 samples.

Because SiO_2 itself exhibited non-negligible photochemistry in our experiments, calculations were slightly more involved for these mixed films.

In order to correct for SiO_2 reactivity, we calculated γ_{BET} (25% RH) for 3 SiO_2 samples with similar masses and used the average γ_{BET} value to back-calculate a γ_{eff} value for the mass of SiO_2 employed in a given TiO_2/SiO_2 experiment. From the γ_{eff} thus obtained, we back-calculated k_{obs} (s^{-1}) for this mass of SiO_2 and subtracted this value from the overall k_{obs} value for the TiO_2/SiO_2 mixed film. In this way, we were able to obtain a k_{obs} value for TiO_2 alone, which we then used to calculate γ_{eff} and γ_{BET} for TiO_2 as described in the previous section. Importantly, we used the total surface area of TiO_2 alone in these calculations, rather than the total surface area of the mixed film. We note that these calculations led to negligible values for k_{obs} of TiO_2 alone under dark conditions; as a result, we do not report dark uptake values for TiO_2.

We note that since radial diffusion limitations are independent of sample type and only depend on overall loss of ozone onto the surface, γ_{eff} values for the TiO_2/SiO_2 mixed films were multiplied by the correction factor ratio associated with γ_{eff} values calculated for the original mixed films (*i.e.* not for the TiO_2 fraction alone).

1.4 Sample treatment, preparation, and characterization

1.4.1 Sample treatment and preparation

Minerals were analyzed for their purity via visual inspection, electron microprobe analysis (EMPA), and X-ray diffraction (XRD). Impurities were identified for each mineral and purification treatments were selected accordingly; a summary of all treatments is

presented in **Table S3**. Pictures of mineral samples prior to treatment and preparation are provided in **Figure S6**.

Obvious impurities on the outside of mineral samples and impurities that could not be removed via chemical treatment (*vide infra*) were removed using a Dremel® tool. Rust was removed by submersing minerals in a 40 g L^{-1} solution of SUPER IRON out® (active ingredients sodium hydrosulfite, sodium metabisulfite, and sodium sulfite) for 30 min. $CaCO_3$ was removed by placing minerals in 1 M HCl (phlogopite, 1.5 hours; titanite 1, 1 day). After the removal of impurities, minerals were rinsed with methanol once and with deionized water 3 times. Minerals that were not subjected to these treatments were also rinsed in this manner.

After minerals underwent purification treatments, they were first broken down using a steel percussion mortar and pestle. To remove any steel contamination from use of the percussion mortar, a rare earth magnet wrapped in weighing paper was then passed over each broken-down sample (this was not possible for ilmenite and hastingsite samples, as they also displayed magnetic properties). Minerals were then ground using an agate mortar and pestle until they had a fine, powder-like appearance. To prevent cross contamination, pure gem-quality Brazilian quartz (from Corinto, Brazil) was used to clean the steel percussion and agate mortar and pestle between samples by grinding the quartz into a fine powder; afterward, grinding equipment was rinsed with ethanol.

1.4.2 Surface area determination

Prior to gas adsorption analysis, samples were degassed (activated) on a gas adsorption sample preparation instrument (Smart VacPrep, Micromeritics); in order to ensure that the measured surface area is reflective of the surface area presented under our experimental conditions, degassing was performed in the absence of heat. For activation, each sample was weighed into a pre-weighed glass sample tube equipped with filler rod and steel frit ball valve. Samples were subsequently activated by evacuating the sample holder at 5.00 mmHg s^{-1} until a pressure level of 1.00 mmHg or lower was achieved; the Smart VacPrep instrument has a needle on the vacuum port to open the ball valve. Subsequently the samples were held under unrestricted vacuum for 24 h. The sample holders were then backfilled with nitrogen gas, removed from the Smart VacPrep instrument, and reweighed. Gas adsorption isotherm data were collected at 77 K using nitrogen gas as the probe molecule (3Flex, Micromeritics). Using the MicroActive software suite, the data obtained were used to determine the Brunauer–Emmett–Teller (BET) accessible surface area by fitting the linear BET equation and ensuring that the 4-point criterion was met[11].

1.4.3 Electron microprobe analysis

Electron microprobe analysis was conducted on 2 separate dates because minerals were purchased in 2 groups. The first set of minerals analyzed consisted of anatase 1, rutile, ilmenite, titanite 1, phlogopite, hastingsite, augite, and epidote. The second set, which was purchased to enable us to study the reactivity of samples of the same mineral obtained from different locations, consisted of anatase 2 and titanite 2. All EMPA data can be found in **Tables S5–14**.

1.4.3.1 Analysis of anatase 1, rutile, ilmenite, titanite 1, phlogopite, hastingsite, augite, and epidote

An electron microprobe (JXA-8900R, JEOL) was used to examine grains of anatase 1, rutile, ilmenite, titanite 1, phlogopite, hastingsite, augite, and epidote, which had been mounted in epoxy, polished, and carbon-coated (25 nm thickness) prior to analysis. In addition to back-scattered electron images, quantitative compositional data were acquired from spot analyses of the minerals using wavelength-dispersive spectrometry and Probe for EPMA software[12]. Thirteen elements were measured (Na, Mg, Al, Si, K, Ca, Ti, V, Cr, Mn, Fe, Zn, and Nb) with the following conditions: 20 kV accelerating voltage, 20 nA probe current, and a 1 μm beam diameter for all minerals except pholgopite, for which a 5 μm beam was used. Total count times of 20 s were used for both peaks and backgrounds for all elements except V, Zn, and Nb, for which 30 s was used. The X-ray lines and diffraction crystals were: Na *K*α, TAP (thallium hydrogen phthalate); Mg *K*α, TAP; Al *K*α, TAP; Si *K*α, TAP; K *K*α, PET (pentaerythritol); Ca *K*α, PET; Ti *K*α, PET; V *K*α, PET; Cr *K*α, PET; Mn *K*α, LIF (lithium fluoride); Fe *K*α, LIF; Zn *K*α, LIF; and Nb *L*α, PET. Corrections were applied to V for interference by Ti, to Cr for interference by V, and to Mn for interference by Cr[13]. X-ray intensity data were reduced following Armstrong (1995)[14]. The reference standards consisted of metals, synthetic inorganic materials, and natural minerals[15].

1.4.3.2 Analysis of anatase 2 and titanite 2

An electron microprobe (SX100, Cameca) was used to examine grains of anatase 2 and titanite 2, which had been mounted in epoxy, polished, and carbon-coated (25 nm thickness) prior to analysis. In addition to back-scattered electron images, quantitative

compositional data were acquired from spot analyses of the minerals using wavelength-dispersive spectrometry and Probe for EPMA software[12]. Thirteen elements were measured (Na, Mg, Al, Si, K, Ca, Ti, V, Cr, Mn, Fe, Zn, and Nb) with the following conditions: 20 kV accelerating voltage, 20 nA probe current, and a 1 μm beam diameter. Total count times of 30 s were used for both peaks and backgrounds for all elements. The X-ray lines and diffraction crystals were: Na *K*α, TAP; Mg *K*α, TAP; Al *K*α, TAP; Si *K*α, TAP; K *K*α, PET; Ca *K*α, PET; Ti *K*α, PET; V *K*α, PET; Cr *K*α, PET; Mn *K*α, LIF; Fe *K*α, LIF; Zn *K*α, LIF; and Nb *L*α, PET. Corrections were applied to V for interference by Ti, to Cr for interference by V, and to Mn for interference by Cr[13]. However, the correction to V was found to be insufficient, based on analysis of reference rutile, and so the V data were discarded. The X-ray intensity data were reduced following Armstrong (1995)[14]. The reference standards consisted of metals, synthetic inorganic materials, and natural minerals[15].

1.4.4 X-ray diffraction analysis

Powder X-ray diffraction (XRD) patterns of the ground mineral samples were collected on a Rigaku Ultima IV diffractometer with a Co *K*α radiation source operated at 38 kV and 38 mA. Phase identification was performed using JADE 9.6 software with the 2019 ICDD Database PDF 4+ and 2018-1 ICSD databases[16,17]. The patterns were analyzed with the TOPAS academic software package[18]. All phases were analyzed with Pawley refinement method[19]. X-Ray diffraction data and refinement fits are shown in **Figures S9–10**. The phases and their statistics from refinement fits are presented in **Table S15**, which also summarizes the results and lists the cell parameters of the refined phases from the powder XRD data.

The refinements in **Figures S9–10** show good visual fits and excellent refinement statistics (**Table S15**). Ilmenite had no observed impurity peaks in its diffraction pattern (**Figure S10**). For the rest of the samples, asterisks indicate the most intense impurities observed with the X-ray diffraction technique. The phlogopite sample exhibited a strong preferred orientation in the 0 0 2*n* direction, which resulted in a strong intensity of the 0 0 2*n* peaks in the powder pattern (**Figure S10**). The samples with major impurity contents (hastingsite and epidote) were also analyzed with Pawley fit to identify the presence of secondary phases (see **Figure S10**).

Powder diffraction of all anatase (TiO_2) samples revealed minor (< 5%) unidentified impurities based on a relative intensity comparison (**Figure S7**). The peak at ~32° 2θ could theoretically be assigned to rutile; the absence of other rutile phase peaks likely reflects the low abundance of this phase. The commercial anatase sample was purchased from a batch with a claimed anatase purity of 99.8%; a minor rutile peak was apparent in a quality check diffraction pattern collected in 2014 (see **Figure S8**). However, **Figure S7** shows multiple other unidentified peaks in the powder diffraction pattern for this sample. Since most of the impurities found in all 3 anatase samples gave reflections at the same diffraction angles, a single crystal was picked from one of the samples (anatase 2) for analysis to check whether these peaks reflected impurities within the phase itself or the existence of additional impurity phases. Similarly, titanite 2 (**Figure S10)** features 2 unassigned peaks in its diffraction pattern that were not present in the diffraction pattern for titanite 1 (**Figure S10**). In order to check if these peaks originated from the structure of this particular sample of titanite, a single crystal was picked from the mineral sample and analyzed via single crystal diffraction.

Single crystal diffraction measurements were accomplished using a Bruker PLATFORM diffractometer equipped with a SMART APEX II CCD area detector and a graphite-monochromated Mo Kα radiation source, using ω scans at 8 different ϕ angles with a frame width of 0.3° and an exposure time of 10 s per frame. Face-indexed absorption corrections were applied[20]. Structure solution and refinement were carried out using the SHELXTL (version 6.12) program package[21]. The results of these analyses are displayed in **Tables 16–20**.

Atomic coordinates and crystallographic details are comparable to other crystallographic reports of anatase and titanite crystals; no structural anomalies were observed. Atomic distances from the crystallographic analysis are similar to multiple single crystal diffraction reports of these minerals. In the case of anatase 2, a small excess of electron density on Ti atom (0.4 $e^-/Å^3$) is in a good agreement with the atomic composition (0.92 Ti + 0.08 Fe) suggested by microprobe analysis (**Table S6**). Additionally, atomic displacement parameters are slightly higher than what would be expected, suggesting negligible mixing in the metal site, which is in a good agreement with the microprobe data. The extra peaks (observed on powder patterns) were absent in the single crystal diffraction data, which suggests that these peaks indeed belonged to impurity phase(s) and/or Kβ diffraction from the anatase phase rather than to structural imperfections of the main phase.

1.4.5 UV-Vis diffuse reflectance spectroscopy

In order to determine the extent to which each Ti-containing mineral sample absorbs light within the transmission range of the UV-A lamps in the photoreactor and to obtain their band gaps, diffuse reflectance spectra were collected using a UV-Vis-NIR

spectrophotometer (Cary, 5000) equipped with a diffuse reflectance accessory. Spectralon® was used as 100% reflectance standard and spectra were measured from 200–800 nm for all minerals except ilmenite, the spectrum of which was measured to 1200 nm, as its absorbance extended into the NIR region. Diffuse reflectance data were transformed using the Kubelka–Munk function[22]:

$$\frac{K}{S} = \frac{(1-R)^2}{2R}$$

Here, K is the absorption coefficient, S is the scattering coefficient, and R is the reflectance. Band gaps for Ti-containing minerals were determined by plotting the Kubelka–Munk function (K/S) against eV, where eV corresponds to the kinetic energy of a single electron at a given wavelength, and then taking the intersection between a linear fit of the reflectance dip and a horizontal line along the baseline of K/S[23]. The Kubelka–Munk plots for a selection of minerals (with associated band gaps, when possible) are presented in **Figure 4**; the remainder of the minerals are shown in **Figure S11**.

1.4.6 Scanning electron microscopy

The size and morphology of a select set of mineral samples—commercial anatase, anatase 1, anatase 2, rutile, titanite 1, and titanite 2—were assessed using a field emission scanning electron microscope (FESEM, Zeiss Sigma). In order to prepare samples for SEM analysis, a small amount (several mg) of each mineral was sprinkled onto carbon tape, which was then mounted on an aluminum stub. To reduce the influence of surface charging from the electron beam, samples were carbon coated using a sputter coater (EM SCD005, Leica).

Secondary electron images were collected using in-lens mode at 10 kV at 1000× magnification, except in the case of commercial anatase, which was obtained at 10,000× magnification due to its significantly smaller particle sizes compared to the natural ground minerals. All secondary electron images are presented in **Figure S12**.

1.5 Chemicals

Natural minerals were sourced from www.minfind.com and through contact with individual vendors. Deionized water (18 MΩ) was obtained from a Millipore Synergy UV ultrapure water system. TiO_2 (anatase, 99.8% trace metal basis), KOH (ACS reagent ≥ 85%, pellets), and chloramine T trihydrate (Reag. Ph. Eur. grade) were obtained from Sigma Aldrich. SiO_2 (amorphous fumed, reported surface area 85–115 $m^2\ g^{-1}$) was obtained from Alfa Aesar. Methanol (Optima grade, 99.9%), 2-propanol (certified ACS Plus), Na_2CO_3 (anhydrous, certified ACS powder), and glycerol (certified ACS) were obtained from Fisher Chemicals. Concentrated H_2SO_4 (reagent grade) and concentrated HCl (reagent grade) were obtained from Caledon Laboratory Chemicals. SUPER IRON out® (Summit Brands) was purchased from Canadian Tire®. Sparkleen™ was purchased from Fisherbrand™. Ethanol (95%) was obtained from Commercial Alcohols. Except for the natural mineral samples, which were treated as described in **Section 1.4.1**, all chemicals were used as received.

2 Supporting results and discussion

2.1 Ozone uptake by Ti-containing minerals under dark conditions

Although the primary focus of this study was the photochemistry of Ti-containing minerals, we also investigated ozone uptake by these minerals under dark conditions. As illustrated in **Figures S3–4,** ozone exhibited time-dependent uptake to most Ti-containing mineral samples under dark conditions. In particular, for most samples, the magnitude of ozone loss decreased with increasing sample exposure and eventually reached a plateau value; in other words, the concentration of ozone at the exit of the flow tube increased with increasing sample exposure and eventually reached a steady state. We note that in some cases, steady-state conditions were not reached *(e.g.* phlogopite, titanite 1, anatase 1, and anatase 2; **Figures S3–4**), as we wanted to keep the total reaction time similar between experiments; for these minerals, therefore, γ_{BET} values represent an upper limit.

As shown in **Figure S14**, γ_{BET} values for our samples under dark conditions were significantly lower than values obtained under illumination. Under dark conditions, γ_{BET} values spanned almost an order of magnitude, with the highest values calculated for ilmenite (7.6×10^{-7}) and the lowest for epidote ($(7.5 \pm 1.8) \times 10^{-8}$). We note that ilmenite displayed 2 distinct types of reaction profiles with associated uptake coefficients ($(6.9 \pm 1.3) \times 10^{-7}$, $n = 3$; $(2.4 \pm 0.6) \times 10^{-7}$, $n = 3$); although we are not currently able to definitively explain this behavior, we tentatively suggest that it may reflect variable contributions from additional minor mineral phases within the sample. If present, these additional mineral phases may have gone undetected during our sample characterization procedures, as EMPA results only reflect the elemental abundances in spot-selected areas of mineral samples and XRD is not always able to detect minor phases in multi-phase samples[24]. To compare the reactivity of our minerals to natural dust samples, we also measured ozone

uptake by Cape Verde dust and Gobi dust; for these samples, γ_{BET} values of $(2.2 \pm 0.2) \times 10^{-8}$ and $(3.6 \pm 0.6) \times 10^{-8}$ were obtained, respectively.

Ozone uptake by TiO_2/SiO_2 mixed films under dark conditions was indistinguishable from that by SiO_2 films, which was itself small. These results agree with the coated-wall flow tube study of Nicolas et al., which reported minimal uptake of ozone by TiO_2/SiO_2 films under dark conditions[3]. As noted in **Section 1.3.3.1**, because of the substantial photoreactivity of TiO_2 samples, our films were prepared using low Ti mass fractions (see **Table S2**), which implies that TiO_2 minerals themselves may be measurably reactive toward ozone under dark conditions; however, this was not the focus of the present study and is not explored/discussed here.

2.1.1 Suggested mechanism for ozone uptake by Ti and Ti-bearing minerals

The following mechanism has been proposed for the interaction of ozone with metal oxide surfaces, where SS represents an active surface site (we note that the importance of **R4** is debated)[25,26]:

$$O_3 + SS \rightarrow SS{-}O + O_2 \quad (1)$$

$$SS{-}O + O_3 \rightarrow SS{-}O_2 + O_2 \quad (2)$$

$$SS{-}O_2 \rightarrow SS + O_2 \quad (3)$$

$$2(SS{-}O) \rightarrow 2\,SS + O_2 \quad (4)$$

The saturation of active surface sites via **R1** and **R2** implies that ozone uptake by these samples will eventually become negligible; however, the mechanism also allows for

regeneration of these sites via **R3** and **R4**, which would lead to sustained (*i.e.* catalytic) ozone loss. Our steady-state ozone concentrations do not return back to their initial values prior to sample exposure (see **Figures S3–4**), which implies that destruction of ozone is catalytic in nature to some degree for all of our samples. This catalytic behavior has been previously observed for several natural mineral dusts[5,9,27] , clays[5,8,29], and metal oxides[3,5,28,30,31], the latter two of which are commonly used as mineral dust proxies.

The surface sites (SS) presented in **R1–4** represent active Lewis acid sites (*i.e.* surface defects in the form of oxygen vacancies) that can promote ozone dissociation and resultant formation of surface-bound oxygen atoms; in fact, in the case of volcanic ash, ozone has been used as a molecular probe for Lewis acid sites[32]. The adsorption of ozone at these Lewis acid sites has been studied using many surface spectroscopic techniques, including FT-IR[33], XPS[34], Raman[26,35,36], and DRIFTS[37]. The degree to which the catalytic destruction of ozone occurs depends greatly on the strength of these Lewis acid sites. For example, previous studies have found that the catalytic uptake of ozone by Fe_2O_3 is greater than by Al_2O_3, which is in turn greater than by SiO_2[5]. This trend has been attributed to Fe_2O_3 having the weakest Lewis acid sites—and, by extension, the weakest SS–O_2 bonds—which allows for greater regeneration of SS[30].

We suggest that similar considerations may be relevant for our sample set, which includes minerals with different chemical compositions and crystal structures (*i.e.* that observed reactivity differences may arise from differences in strength of Lewis acid sites). For example, ilmenite's elevated dark reactivity compared to other samples may reflect its elevated Fe content (~45%, **Table S8**) and consequent availability of Fe cations at its

509 surface. In addition, titanite 1's reactivity (γ_{BET} = (1.29 ± 0.02) × 10^{-7}) compared to titanite 2
510 (uptake negligible compared to controls, and therefore not reported) may reflect the 4×
511 larger amount of Fe detected in the former sample (**Tables S9–10**).

512 Fe can easily substitute for Ti in mineral structures due to its similar cation size and
513 charge[38]. Depending on formation processes and conditions (*e.g.* crystallization
514 environment), therefore, we expect titanium-containing minerals in the environment to
515 have different abundances of these elements in their crystal structures, and ultimately
516 exhibit different reactivities; in other words, we anticipate that the results obtained here
517 are not specific for titanite but rather reflective of broader variability in environmental
518 samples.

519 **2.1.2 Comparison of uptake coefficients to previous literature**

520 Previous laboratory studies investigating the uptake of ozone by natural mineral dusts and
521 mineral dust proxies have been conducted using coated-wall flow tubes[8,25,29,39],
522 environmental chambers[30,31], and Knudsen cells[5,27,28]. Detailed descriptions of these
523 systems are provided in a review by Kolb et al.[40], but the most significant difference
524 between them is that whereas Knudsen cells are operated under molecular flow conditions
525 (*i.e.* under vacuum), coated-wall flow tubes and environmental chambers can be operated
526 at atmospheric pressures.

527 Uptake coefficients reported in Knudsen cell studies of dust–ozone interactions are
528 significantly larger than those obtained in this work. For example, Hanisch and Crowley
529 reported a steady-state BET uptake coefficient of 7 × 10^{-6} for the uptake of ozone by

530 Saharan Desert dust[41], which is ~9–90× larger than the values obtained in our experiments
531 for our natural Ti-containing mineral samples and 200–300× larger than our Gobi and
532 Saharan dust samples, respectively. In the following paragraph, we suggest three
533 possibilities to explain this discrepancy.

534 First, as recently discussed by Lasne et al., the larger ozone uptake coefficients obtained in
535 Knudsen cell experiments could potentially be explained by more favorable regeneration of
536 surface sites via decomposition of SS–O_2 (**R3**) at lower operating pressures[8]. Second, as
537 noted by Coates Fuentes et al., who reported smaller ozone uptake coefficients for clays in
538 their coated-wall flow tube experiments as compared to previous values from Knudsen cell
539 experiments, the *in situ* BET surface area of samples may differ from that measured when
540 samples are present in powder form[29]. A reduction in the actual BET surface area of our
541 coated tubes with respect to the values determined for dry samples would also lead to an
542 underestimation in our calculated γ_{BET} values. In the case of ozone uptake by hydrocarbon
543 soot, *in situ* gas adsorption analysis[42] has previously been used to address these issues;
544 however, this approach would be challenging for our samples, which have significantly
545 lower specific surface areas. Third, we show in **Section 2.1.3** for a subset of our mineral
546 samples that the uptake of ozone decreases with increasing RH. By extension, we might
547 expect uptake coefficients to be higher in low-pressure reactors, where adsorbed water
548 may be more thoroughly removed from samples and the number of available surface sites
549 for ozone adsorption may be correspondingly increased.

550 Uptake coefficients derived from studies conducted at atmospheric pressure are in better
551 agreement with our values[3,8,25,29–31]. For example, Mogili et al. investigated ozone uptake

552 onto α-Al_2O_3 and α-Fe_2O_3 as a function of RH and ozone partial pressure in an atmospheric
553 chamber and obtained γ_{BET} values ranging from 1.9×10^{-9} to 1.3×10^{-7} for these samples[30].
554 In addition, Coates Fuentes et al. studied ozone uptake onto kaolinite, a clay used as a
555 mineral dust proxy, using a coated-wall flow tube and found a γ_{BET} value of 1.9×10^{-8} at RH
556 <1% [29]; similar results were obtained by Lasne et al.[8]. Finally, our results for Gobi dust are
557 similar to those reported in a previous study of the catalytic uptake of ozone by this
558 substrate in a U-shape fixed-bed reactor[9].

559 **2.1.3 Influence of relative humidity on ozone uptake**

560 Although mineral dust is emitted primarily in arid regions, it can be exposed to
561 environments of differing RH during atmospheric transport. For example, mineral dust is
562 primarily transported across the Atlantic Ocean in the Saharan Air Layer, a dry, warm, air
563 mass; during transport, however, tropical disturbances can lead to vertical mixing of this
564 layer with underlying cool, moist, tropical Atlantic air and ultimately expose dust to more
565 humid environmental conditions[43,44]. In addition, the mixing between dry, dust-laden air
566 flows and more humid air can also occur during dust storm episodes that occur at lower
567 altitudes[45]. In this context, it is important to understand the influence of water vapour on
568 the reactivity of our samples toward ozone.

569 Here, we investigated the RH dependence of ozone uptake for all TiO_2 minerals studied
570 (commercial anatase, anatase 1, anatase 2, and rutile) and for 4 Ti-containing minerals
571 (titanite 1, titanite 2, phlogopite, and ilmenite). Because we observed minimal loss of ozone
572 for all TiO_2/SiO_2 samples under dark conditions, discussion of the influence of RH on ozone
573 uptake by these samples is presented in **Section 2.2.3** (illuminated conditions). In the case

of titanite 2, dark reactivity was small at all RH values (results not shown), so trends in uptake were difficult to discern. In the case of ilmenite, the bimodal reactivity described in **Section 2.1** precluded reliable interpretation of RH trends. For these reasons, we limit our discussion to the influence of RH on ozone uptake by titanite 1 and phlogopite.

As illustrated in **Figure S5**, the loss of ozone at the surface of both titanite 1 and phlogopite increased with decreasing RH. At lower RH values, the correction factor for radial diffusion of ozone inside the coated-wall flow tube becomes very large; for this reason, we did not calculate γ_{BET} values for these experiments. These results agree qualitatively with those obtained in previous studies of ozone uptake by metal oxides[25,25,31] and clays[8,29], and most likely reflect competition by water vapour for available surface sites for ozone adsorption[46].

2.2 Ozone uptake by TiO_2 under illuminated conditions

2.2.1 Mechanistic discussion for photoenhanced ozone uptake by TiO_2

Here, we elaborate on the mechanism proposed by Nicolas et al. for the TiO_2-catalyzed uptake of ozone (**R5–R13**)[47]:

$$TiO_2 + h\nu \rightarrow TiO_2\,(e^- + h^+) \quad (5)$$

$$O_3 + e^- \rightarrow O_3^{\bullet-} \quad (6)$$

$$O_2 + e^- \rightarrow O_2^{\bullet-} \quad (7)$$

$$O_2^{\bullet-} + O_3 \rightarrow O_3^{\bullet-} + O_2 \quad (8)$$

$$O_3^{\bullet-} + H^+ \rightarrow HO_3^{\bullet} \quad (9)$$

$$HO_3^{\bullet} \rightarrow O_2 + {}^{\bullet}OH \quad (10)$$

$${}^{\bullet}OH + O_3 \rightarrow O_2 + HO_2^{\bullet} \quad (11)$$

$$H_2O_{(ads)} + h^+ \rightarrow 2\ {}^{\bullet}OH \quad (12)$$

$$>TiOH + h^+ \rightarrow \{>TiOH^{\bullet}\}^+ \quad (13)$$

In this mechanism, absorption of light with energy equal to or greater than the band gap of TiO_2 leads to the formation of an electron–hole pair (**R5**) and initiates a chain of reactions that reduce ozone and ultimately result in the release of molecular oxygen (**R6–R11**). In this proposed mechanism, ozone can be reduced directly by photogenerated electrons (**R6**) or indirectly by superoxide radicals produced from the reduction of molecular oxygen by photogenerated electrons (**R7–8**). In both cases, the ozonide radical thus produced can decompose to yield hydroxyl radicals (**R9–10**), which can in turn lead to further ozone decomposition (**R11**). Under our experimental conditions, additional mechanisms for hydroxyl radical production include the reaction of photogenerated holes with molecularly adsorbed water (**R12**) and/or the hydrated surface of TiO_2 (**R13**)[48].

2.2.2 Comparison of uptake coefficients to previous literature

Although this work is the first to study the photochemical uptake of ozone by natural Ti-containing minerals, several other studies have explored the photochemical uptake of ozone by commercial TiO_2. Using a coated-wall flow tube, Nicolas et al. obtained a γ_{BET} value of $(2.6 \pm 0.4) \times 10^{-6}$ for TiO_2/SiO_2 mixed films at similar ozone concentrations, RH values,

613 and film masses to those employed in our experiments[47]. This value is much lower than the
614 value we obtain in this work (*i.e.* $(1.8 \pm 0.3) \times 10^{-4}$). We suggest that this difference may
615 reflect different approaches used to calculate γ_{BET}: specifically, because these authors were
616 interested in the reactivity of the composite film rather than the reactivity of TiO_2 itself,
617 they reported γ_{BET} values corrected for the entire surface area of their TiO_2/SiO_2 mixed
618 films. By contrast, in this work, because we were interested in obtaining γ_{BET} for the TiO_2
619 fraction, we used the surface area of TiO_2 alone in our calculations (see **Section 1.3.3.1**). In
620 another study, Chen et al.[31] used an environmental reaction chamber to obtain a γ_{BET} value
621 of $(2.4 \pm 0.1) \times 10^{-7}$, which is lower than both the values obtained in this study and those
622 reported by Nicolas et al.[31]. We suggest that this discrepancy likely reflects the use of
623 significantly higher ozone concentrations in the reaction chamber than in the flow tube
624 studies, as calculated γ_{BET} values for surface-mediated reactions display a negative
625 dependence on gas-phase ozone concentrations[47]. Finally, whereas our commercial TiO_2
626 was primarily anatase, the two previous studies used Degussa TiO_2, which contains both
627 anatase and rutile. Since studies have shown that the photoreactivity of mixed TiO_2 phases
628 can differ from that of individual TiO_2 phases[49] , it is also possible that the inherent
629 photoreactivity of our TiO_2 sample differs from those employed in these previous studies.

630 **2.2.3 Influence of relative humidity on ozone uptake**

631 In order to assess the influence of adsorbed water on the photochemical uptake of ozone by
632 our TiO_2 samples, we performed experiments at several RH values. As illustrated in **Figure**
633 **S13**, anatase 1 exhibits the highest photoreactivity at RH 10%. These results agree with
634 those of Nicolas et al., who observed the highest photoreactivity values for TiO_2 with ozone

635 at intermediate RH values[47]. They attributed lower photoreactivities under wet conditions
636 to competitive adsorption by water vapour, and lower photoreactivities under dry
637 conditions to reductions in the quantity of adsorbed water available to generate radical
638 species ((**R12**) in the mechanism described in **Section 2.2.1**) at the illuminated TiO_2
639 surface[47,51]. The fact that photochemistry still occurs under dry conditions in both of our
640 studies implies that the hydrated TiO_2 surface itself may also participate in photochemistry
641 (**R13**); additional evidence for photochemistry in the absence of water vapour is also
642 provided by observations of TiO_2-mediated photochemistry under vacuum conditions (*i.e.*
643 in a photochemical Knudsen cell)[52].

644 **Figure S13** also shows that the trends in γ_{BET} as a function of RH are mineral-dependent
645 for our sample set: specifically, commercial anatase and anatase 2 display the highest
646 photoreactivity at RH <0.1%, whereas the photoreactivity of rutile is relatively invariant
647 with RH. If the two competing mechanisms described by Nicolas et al.[47] are also in
648 operation for our samples, these discrepancies imply that our samples may differ in their
649 degree of inherent hydration and/or their ability to retain residual water during our
650 (relatively mild) sample drying process[53]. These results again highlight the complexities
651 associated with photochemistry at the surface of natural samples, and that observations
652 obtained for model systems may not be directly applicable to all environmental substrates.

3 References

(1) Parrish, D. D.; Murphy, P. C.; Albritton, D. L.; Fehsenfeld, F. C. The Measurement of the Photodissociation Rate of NO2 in the Atmosphere. *Atmos. Environ.* **1983**, *17* (7), 1365–1379. https://doi.org/10.1016/0004-6981(83)90411-0.

(2) Zafonte, L.; Rieger, P. L.; Holmes, J. R. Nitrogen Dioxide Photolysis in the Los Angeles Atmosphere. *Environ. Sci. Technol.* **1977**, *11* (5), 483–487.

(3) Nicolas, M.; Ndour, M.; Ka, O.; D'Anna, B.; George, C. Photochemistry of Atmospheric Dust: Ozone Decomposition on Illuminated Titanium Dioxide. *Environ. Sci. Technol.* **2009**, *43* (19), 7437–7442. https://doi.org/10.1021/es901569d.

(4) Pöschl, U.; Rudich, Y.; Ammann, M. Kinetic Model Framework for Aerosol and Cloud Surface Chemistry and Gas-Particle Interactions–Part 1: General Equations, Parameters, and Terminology. *Atmos. Chem. Phys.* **2007**, *7* (23), 5989–6023.

(5) Michel, A. E.; Usher, C. R.; Grassian, V. H. Reactive Uptake of Ozone on Mineral Oxides and Mineral Dusts. *Atmos. Environ.* **2003**, *37* (23), 3201–3211. https://doi.org/10.1016/S1352-2310(03)00319-4.

(6) Adams, J. W.; Rodriguez, D.; Cox, R. A. The Uptake of SO2 on Saharan Dust: A Flow Tube Study. *Atmos. Chem. Phys.* **2005**, *5* (10), 2679–2689.

(7) El Zein, A.; Bedjanian, Y. Interaction of NO2 with TiO2 Surface under UV Irradiation: Measurements of the Uptake Coefficient. *Atmos. Chem. Phys.* **2012**, *12* (2), 1013–1020. https://doi.org/10.5194/acp-12-1013-2012.

(8) Lasne, J.; Romanias, M. N.; Thevenet, F. Ozone Uptake by Clay Dusts under Environmental Conditions. *ACS Earth Space Chem.* **2018**, *2* (9), 904–914. https://doi.org/10.1021/acsearthspacechem.8b00057.

(9) Wang, X.; Romanias, M. N.; Thévenet, F.; Rousseau, A. Geocatalytic Uptake of Ozone onto Natural Mineral Dust. *Catalysts* **2018**, *8* (7), 263. https://doi.org/10.3390/catal8070263.

(10) Knopf, D. A.; Pöschl, U.; Shiraiwa, M. Radial Diffusion and Penetration of Gas Molecules and Aerosol Particles through Laminar Flow Reactors, Denuders, and Sampling Tubes. *Anal. Chem.* **2015**, *87* (7), 3746–3754. https://doi.org/10.1021/ac5042395.

(11) Sing, K. S. W. Adsorption by Powders and Porous Solids. In *Adsorption by Powders and Porous Solids (Second Edition)*; Rouquerol, F., Rouquerol, J., Sing, K. S. W., Llewellyn, P., Maurin, G., Eds.; Academic Press: Oxford, 2014; pp 237–268. https://doi.org/10.1016/B978-0-08-097035-6.00007-3.

(12) Donovan, J. J.; Kremser, D.; Fournelle, J. H.; Goemann, K. *Probe for EPMA: Acquisition, Automation and Analysis, Version 11*; Eugene, Oregon, Probe Software, Inc., 2015.

(13) Donovan, J. J.; Snyder, D. A.; Rivers, M. L. *An Improved Interference Correction for Trace Element Analysis*, 2nd ed.; Microbeam Analysis, 1993.

(14) Armstrong, J. T. *CITZAF: A Package of Correction Programs for the Quantitative Electron Microbeam X-Ray-Analysis of Thick Polished Materials, Thin-Films, and Particles*; Microbeam Analysis 4, 1995.

(15) Jarosewich, E.; Nelen, J. A.; Norberg, J. A. *Reference Samples for Electron Microprobe Analysis*, 4th ed.; Geostand. Geoanal. Res, 1980.

(16) Gates-Rector, S.; Blanton, T. The Powder Diffraction File: A Quality Materials Characterization Database. *Powder Diffraction* **2019**, *34* (4), 352–360. https://doi.org/10.1017/S0885715619000812.

(17) Jade 9.5; Materials Data: Livermore, CA. 2019.

(18) TOPAS V4: General Profile and Structure Analysis Software for Powder Diffraction Data. - User's Manual, Bruker AXS, Karlsruhe, Germany. Bruker AXS (2008).

(19) Pawley, G. S. Unit-Cell Refinement from Powder Diffraction Scans. *J. Appl. Cryst.* **1981**, *14* (6), 357–361. https://doi.org/10.1107/S0021889881009618.

(20) Bruker AXS Inc. *Version, S. A. D. A. B. S.*; Madison WI, USA, 2001.
(21) Sheldrick, G. M. SHELXTL, Version 6.12. Bruker AXS Inc.: Madison, WI 2001.
(22) Kortüm, G. *Reflectance Spectroscopy: Principles, Methods, Applications*; Springer Science & Business Media, 2012.
(23) Murphy, A. B. Band-Gap Determination from Diffuse Reflectance Measurements of Semiconductor Films, and Application to Photoelectrochemical Water-Splitting. *Sol. Energy Mater. Sol. Cell* **2007**, *91* (14), 1326–1337. https://doi.org/10.1016/j.solmat.2007.05.005.
(24) Jenkins, R.; Snyder, R. *Introduction to X-Ray Powder Diffractometry*; Wiley: New York, 1996.
(25) Sullivan, R. C.; Thornberry, T.; Abbatt, J. P. D. Ozone Decomposition Kinetics on Alumina: Effects of Ozone Partial Pressure, Relative Humidity and Repeated Oxidation Cycles. *Atmos. Chem. Phys.* **2004**, *4* (5), 1301–1310. https://doi.org/10.5194/acp-4-1301-2004.
(26) Li, W.; Gibbs, G. V.; Oyama, S. T. Mechanism of Ozone Decomposition on a Manganese Oxide Catalyst. 1. In Situ Raman Spectroscopy and Ab Initio Molecular Orbital Calculations. *J. Am. Chem. Soc.* **1998**, *120* (35), 9041–9046. https://doi.org/10.1021/ja981441+.
(27) Hanisch, F.; Crowley, J. N. Ozone Decomposition on Saharan Dust: An Experimental Investigation. *Atmos. Chem. Phys.* **2003**, *3* (1), 119–130. https://doi.org/10.5194/acp-3-119-2003.
(28) Michel A. E.; Usher C. R.; Grassian V. H. Heterogeneous and Catalytic Uptake of Ozone on Mineral Oxides and Dusts: A Knudsen Cell Investigation. *Geophys. Res. Lett.* **2002**, *29* (14), 10–11. https://doi.org/10.1029/2002GL014896.
(29) Coates Fuentes, Z. L.; Kucinski, T. M.; Hinrichs, R. Z. Ozone Decomposition on Kaolinite as a Function of Monoterpene Exposure and Relative Humidity. *ACS Earth Space Chem.* **2017**. https://doi.org/10.1021/acsearthspacechem.7b00107.
(30) Mogili, P. K.; Kleiber, P. D.; Young, M. A.; Grassian, V. H. Heterogeneous Uptake of Ozone on Reactive Components of Mineral Dust Aerosol: An Environmental Aerosol Reaction Chamber Study. *J. Phys. Chem. A* **2006**, *110* (51), 13799–13807. https://doi.org/10.1021/jp063620g.
(31) Chen, H.; Stanier, C. O.; Young, M. A.; Grassian, V. H. A Kinetic Study of Ozone Decomposition on Illuminated Oxide Surfaces. *J. Phys. Chem. A* **2011**, *115* (43), 11979–11987. https://doi.org/10.1021/jp208164v.
(32) Maters, E. C.; Delmelle, P.; Rossi, M. J.; Ayris, P. M.; Bernard, A. Controls on the Surface Chemical Reactivity of Volcanic Ash Investigated with Probe Gases. *Earth Planet. Sci. Lett.* **2016**, *450*, 254–262. https://doi.org/10.1016/j.epsl.2016.06.044.
(33) Bulanin, K. M.; Lavalley, J. C.; Tsyganenko, A. A. IR Spectra of Adsorbed Ozone. *Colloids Surf. A Physicochem. Eng. Asp.* **1995**, *101* (2), 153–158. https://doi.org/10.1016/0927-7757(95)03130-6.
(34) Lampimäki, M.; Zelenay, V.; Křepelová, A.; Liu, Z.; Chang, R.; Bluhm, H.; Ammann, M. Ozone-Induced Band Bending on Metal-Oxide Surfaces Studied under Environmental Conditions. *ChemPhysChem* **2013**, *14* (11), 2419–2425. https://doi.org/10.1002/cphc.201300418.
(35) Li, W.; Oyama, S. T. Mechanism of Ozone Decomposition on a Manganese Oxide Catalyst. 2. Steady-State and Transient Kinetic Studies. *J. Am. Chem. Soc.* **1998**, *120* (35), 9047–9052. https://doi.org/10.1021/ja9814422.
(36) Radhakrishnan, R.; Oyama, S. T. Ozone Decomposition over Manganese Oxide Supported on ZrO2 and TiO2: A Kinetic Study Using in Situ Laser Raman Spectroscopy. *J. Catal.* **2001**, *199* (2), 282–290. https://doi.org/10.1006/jcat.2001.3167.
(37) Roscoe, J. M.; Abbatt, J. P. D. Diffuse Reflectance FTIR Study of the Interaction of Alumina Surfaces with Ozone and Water Vapor. *J. Phys. Chem. A* **2005**, *109* (40), 9028–9034. https://doi.org/10.1021/jp050766r.
(38) Fitzpatrick, R. W.; Chittleborough, D. J. Titanium and Zirconium Minerals. In *Soil Mineralogy with Environmental Applications*; John Wiley & Sons, Ltd, 2002; pp 667–690. https://doi.org/10.2136/sssabookser7.c22.

(39) Chang, R. Y.-W.; Sullivan, R. C.; Abbatt, J. P. D. Initial Uptake of Ozone on Saharan Dust at Atmospheric Relative Humidities. *Geophys. Res. Lett.* **2005**, *32* (14), L14815. https://doi.org/10.1029/2005GL023317.

(40) Kolb, C. E.; Cox, R. A.; Abbatt, J. P. D.; Ammann, M.; Davis, E. J.; Donaldson, D. J.; Garrett, B. C.; George, C.; Griffiths, P. T.; Hanson, D. R.; Kulmala, M.; McFiggans, G.; Pöschl, U.; Riipinen, I.; Rossi, M. J.; Rudich, Y.; Wagner, P. E.; Winkler, P. M.; Worsnop, D. R.; O' Dowd, C. D. An Overview of Current Issues in the Uptake of Atmospheric Trace Gases by Aerosols and Clouds. *Atmospheric Chemistry and Physics* **2010**, *10* (21), 10561–10605. https://doi.org/10.5194/acp-10-10561-2010.

(41) Hanisch, F.; Crowley, J. N. Ozone Decomposition on Saharan Dust: An Experimental Investigation. *Atmos. Chem. Phys.* **2003**, *3* (1), 119–130. https://doi.org/10.5194/acp-3-119-2003.

(42) Aubin, D. G.; Abbatt, J. P. D. Interaction of NO2 with Hydrocarbon Soot: Focus on HONO Yield, Surface Modification, and Mechanism. *J Phys Chem A* **2007**, *111* (28), 6263–6273. https://doi.org/10.1021/jp068884h.

(43) Wu, L. Impact of Saharan Air Layer on Hurricane Peak Intensity. *Geophys. Res. Lett.* **2007**, *34* (9). https://doi.org/10.1029/2007GL029564.

(44) Perry, K. D.; Cahill, T. A.; Eldred, R. A.; Dutcher, D. D.; Gill, T. E. Long-Range Transport of North African Dust to the Eastern United States. *J. Geophys. Res.* **1997**, *102* (D10), 11225–11238. https://doi.org/10.1029/97JD00260.

(45) Xie, C.; Nishizawa, T.; Sugimoto, N.; Matsui, I.; Wang, Z. Characteristics of Aerosol Optical Properties in Pollution and Asian Dust Episodes over Beijing, China. *Appl. Opt.* **2008**, *47* (27), 4945–4951. https://doi.org/10.1364/AO.47.004945.

(46) Rubasinghege, G.; H. Grassian, V. Role(s) of Adsorbed Water in the Surface Chemistry of Environmental Interfaces. *Chem. Commun.* **2013**, *49* (30), 3071–3094. https://doi.org/10.1039/C3CC38872G.

(47) Nicolas, M.; Ndour, M.; Ka, O.; D'Anna, B.; George, C. Photochemistry of Atmospheric Dust: Ozone Decomposition on Illuminated Titanium Dioxide. *Environ. Sci. Technol.* **2009**, *43* (19), 7437–7442. https://doi.org/10.1021/es901569d.

(48) Hoffmann, M. R.; Martin, S. T.; Choi, W.; Bahnemann, D. W. Environmental Applications of Semiconductor Photocatalysis. *Chem. Rev.* **1995**, *95* (1), 69–96. https://doi.org/10.1021/cr00033a004.

(49) Hurum, D. C.; Agrios, A. G.; Gray, K. A.; Rajh, T.; Thurnauer, M. C. Explaining the Enhanced Photocatalytic Activity of Degussa P25 Mixed-Phase TiO_2 Using EPR. *J. Phys. Chem. B* **2003**, *107* (19), 4545–4549. https://doi.org/10.1021/jp0273934.

(50) Bickley, R. I.; Gonzalez-Carreno, T.; Lees, J. S.; Palmisano, L.; Tilley, R. J. D. A Structural Investigation of Titanium Dioxide Photocatalysts. *J. Solid State Chem.* **1991**, *92* (1), 178–190. https://doi.org/10.1016/0022-4596(91)90255-G.

(51) Folli, A.; Campbell, S. B.; Anderson, J. A.; Macphee, D. E. Role of TiO2 Surface Hydration on NO Oxidation Photo-Activity. *J .Photoch. Photobio. A* **2011**, *220* (2), 85–93. https://doi.org/10.1016/j.jphotochem.2011.03.017.

(52) Styler, S. A.; Donaldson, D. J. Photooxidation of Atmospheric Alcohols on Laboratory Proxies for Mineral Dust. *Environ. Sci. Technol.* **2011**, *45* (23), 10004–10012. https://doi.org/10.1021/es202263q.

(53) Brown, G. E.; Henrich, V. E.; Casey, W. H.; Clark, D. L.; Eggleston, C.; Felmy, A.; Goodman, D. W.; Grätzel, M.; Maciel, G.; McCarthy, M. I.; Nealson, K. H.; Sverjensky, D. A.; Toney, M. F.; Zachara, J. M. Metal Oxide Surfaces and Their Interactions with Aqueous Solutions and Microbial Organisms. *Chem. Rev.* **1999**, *99* (1), 77–174. https://doi.org/10.1021/cr980011z.

(54) Ivanov, A. V.; Trakhtenberg, S.; Bertram, A. K.; Gershenzon, Y. M.; Molina, M. J. OH, HO2, and Ozone Gaseous Diffusion Coefficients. *J. Phys. Chem. A* **2007**, *111* (9), 1632–1637. https://doi.org/10.1021/jp066558w.

(55) Jennings, S. G. The Mean Free Path in Air. *J. Aerosol Sci* **1988**, *19* (2), 159–166. https://doi.org/10.1016/0021-8502(88)90219-4.

4 Supporting figures and tables

Figure S1

Schematic of the photochemical coated-wall flow tube reactor, with a) the movable injector pushed in, which prevents the interaction of ozone with mineral samples and b) the movable injector pulled back, which allows for interaction between ozone and mineral samples. For clarity, only 2 of the 4 UV-A lamps in the apparatus are shown here.

a)

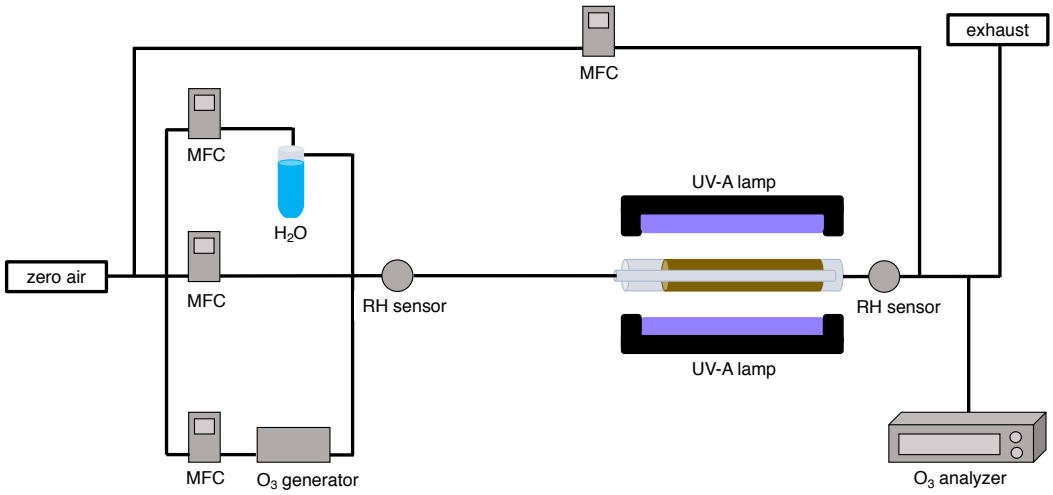

b)

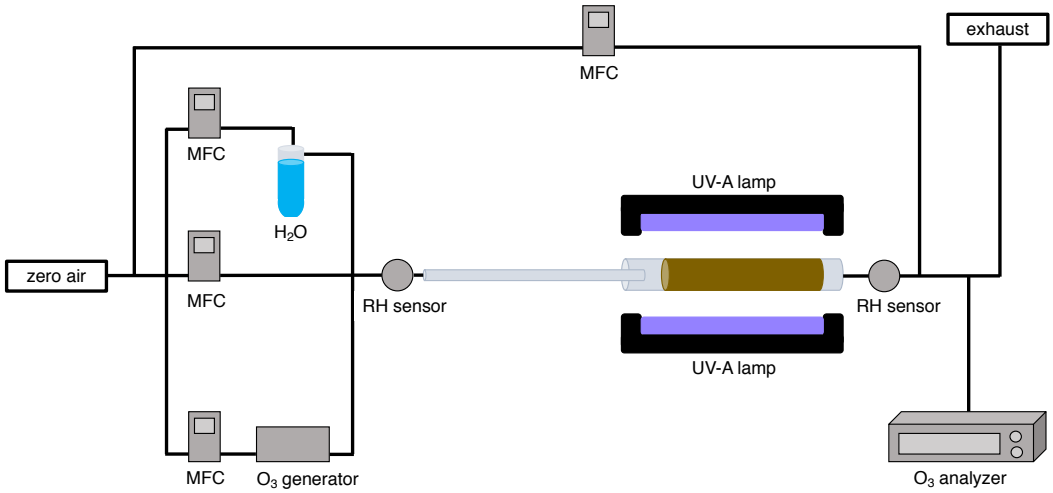

Figure S2

Photolysis frequencies for NO_2 (J_{NO_2}) inside the flow tube versus the number of lamps turned on. Each data point represents the mean of 3 experimental trials, with 1σ error bars; in some cases, error bars are too small to be seen. The dashed line is a linear fit to the experimental data.

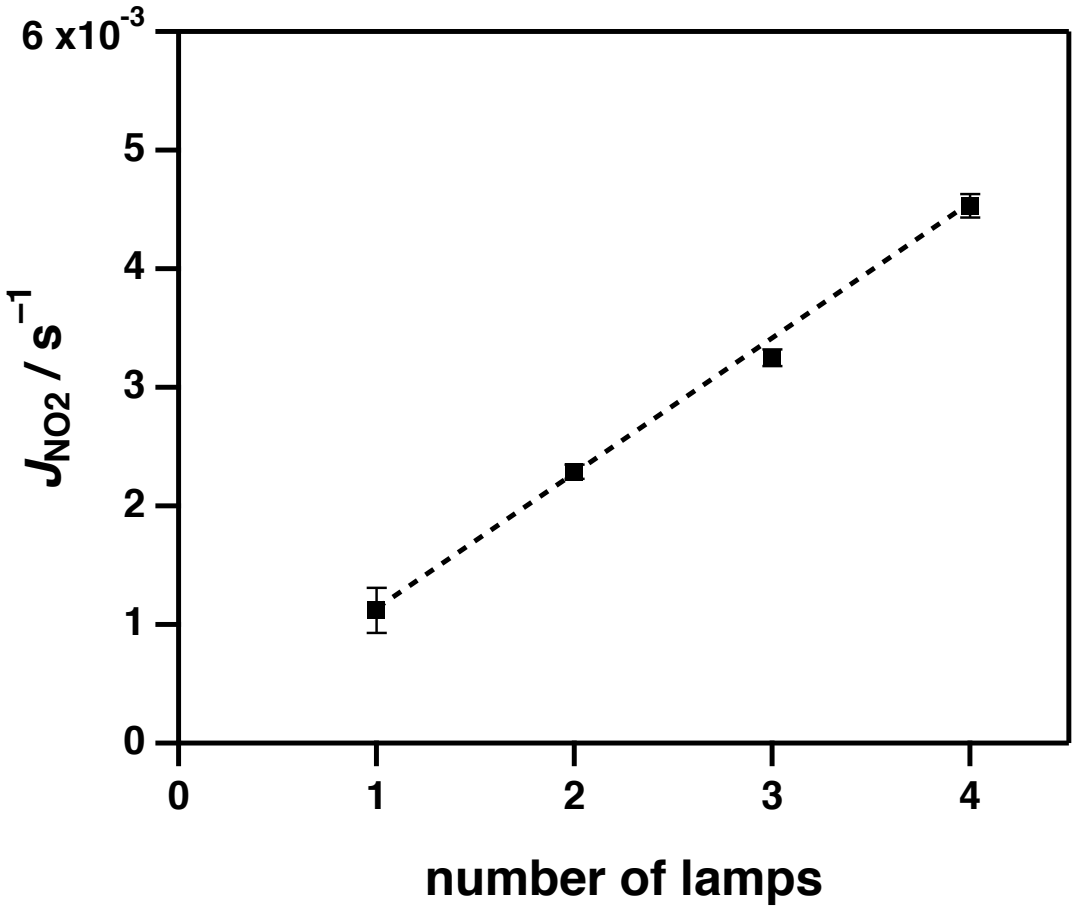

Figure S3

Representative reaction profiles of Ti-containing minerals with ozone at 25% RH. The unshaded regions of the profile show time periods in which ozone was not exposed to our Ti-containing mineral. The blue and yellow regions of the profile show the exposure of ozone to our Ti-containing mineral under dark and illuminated conditions, respectively: a) ilmenite, b) titanite 1, c) titanite 2, d) phlogopite, e) hastingsite, f) augite, and g) epidote.

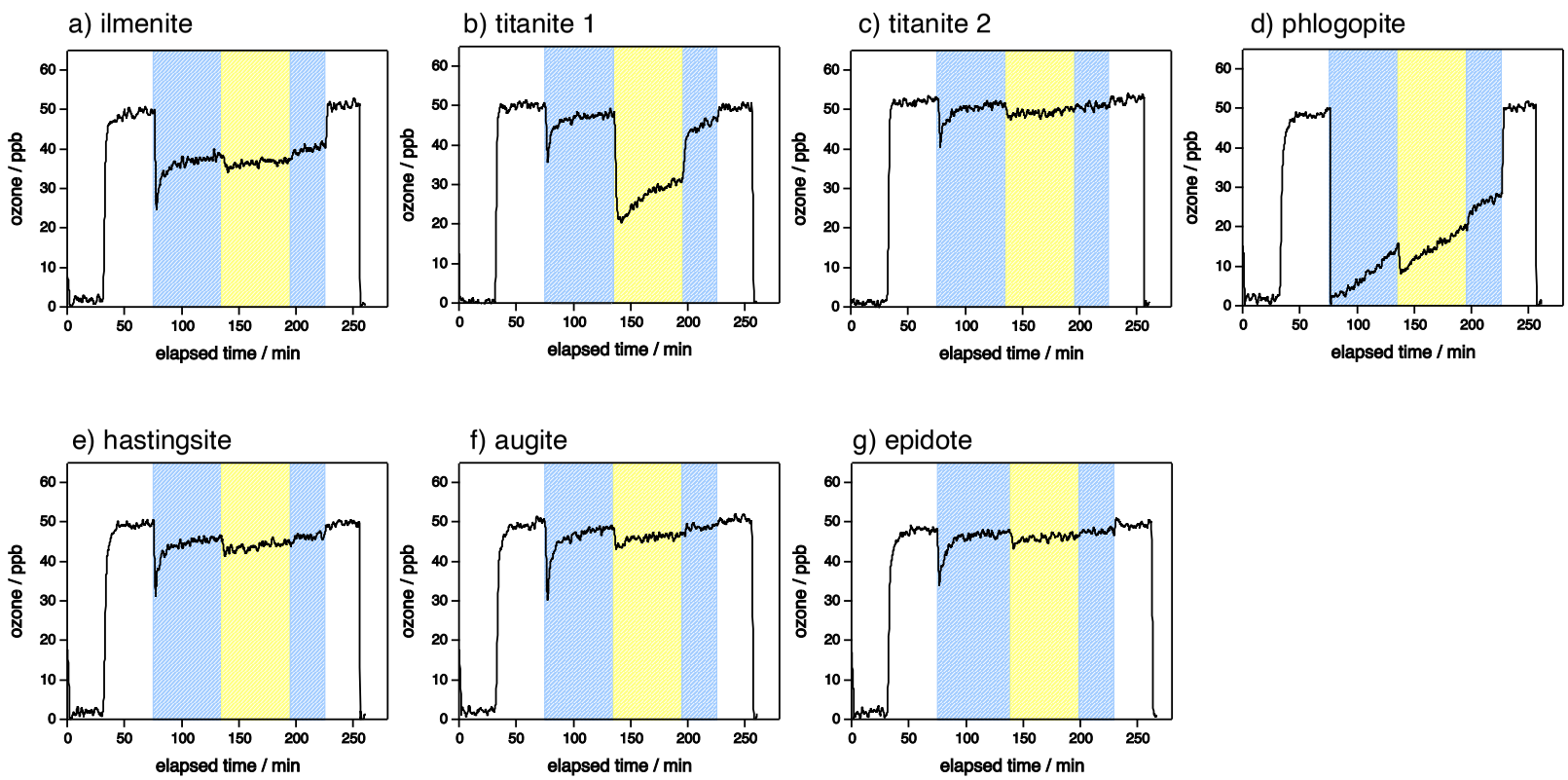

Figure S4
Representative reaction profiles of TiO_2/SiO_2 mixtures with ozone at 25% RH. The unshaded regions of the profile show time periods in which ozone was not exposed to our Ti-containing mineral. The blue and yellow regions of the profile show the exposure of ozone to our Ti-containing mineral under dark and illuminated conditions, respectively: a) commercial anatase (0.1 wt. %), b) anatase 1 (1 wt. %), c) anatase 2 (20 wt. %), and d) rutile (10 wt. %).

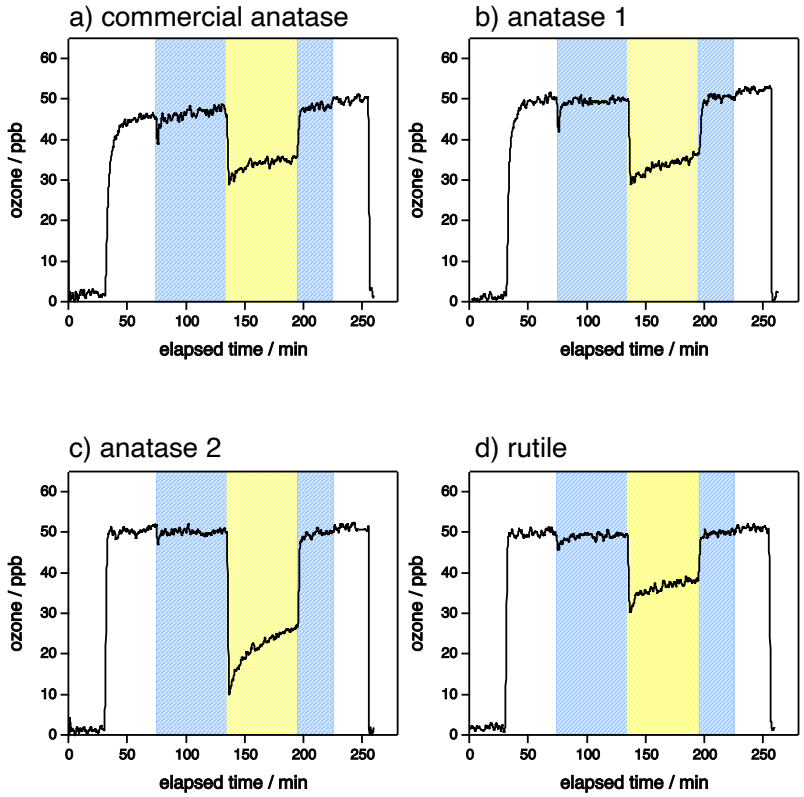

Figure S5
Reaction profiles of selected Ti-containing minerals with ozone as a function of RH. The unshaded regions of the profile show time periods in which ozone was not exposed to our Ti-containing mineral. The blue and yellow regions of the profile show the exposure of ozone to our Ti-containing mineral under dark and illuminated conditions, respectively: a) titanite 1 and b) phlogopite.

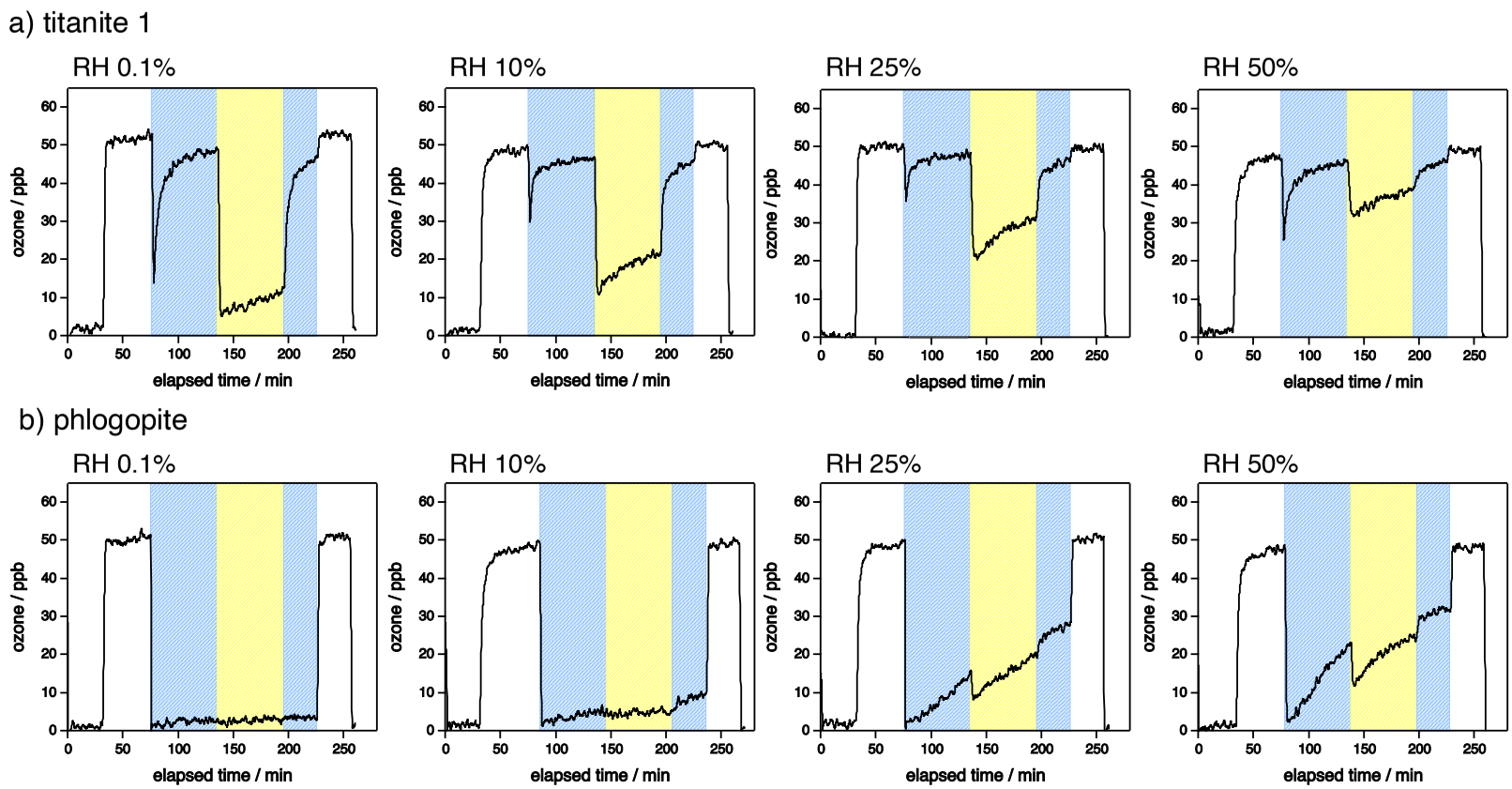

Figure S6
Photographs of natural Ti-containing minerals prior to grinding, with countries of origin listed in parentheses.

anatase 1 (Pakistan) | anatase 2 (Brazil) | rutile (Brazil) | ilmenite (United States) | titanite 1 (Canada)

titanite 2 (Brazil) | phlogopite (Canada) | hastingsite (United States) | augite (United States) | epidote (Norway)

Figure S7
Comparison of powder diffraction data of commercial anatase, anatase 1, and anatase 2. Impurity peaks and/or peaks from Kβ radiation are indicated with arrows.

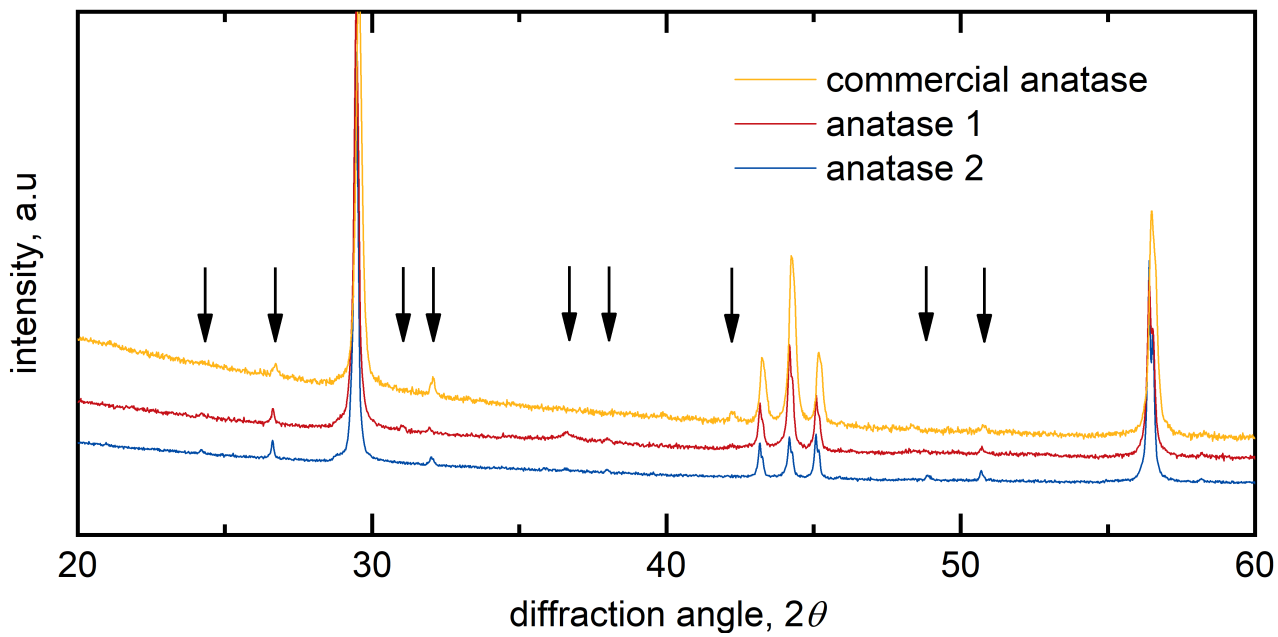

Figure S8
Anatase purity check from Sigma Aldrich. The pattern is from the same batch as our commercial anatase sample. Cu radiation source was used for this measurement. Minor rutile peak is at 27.3° 2θ angle.

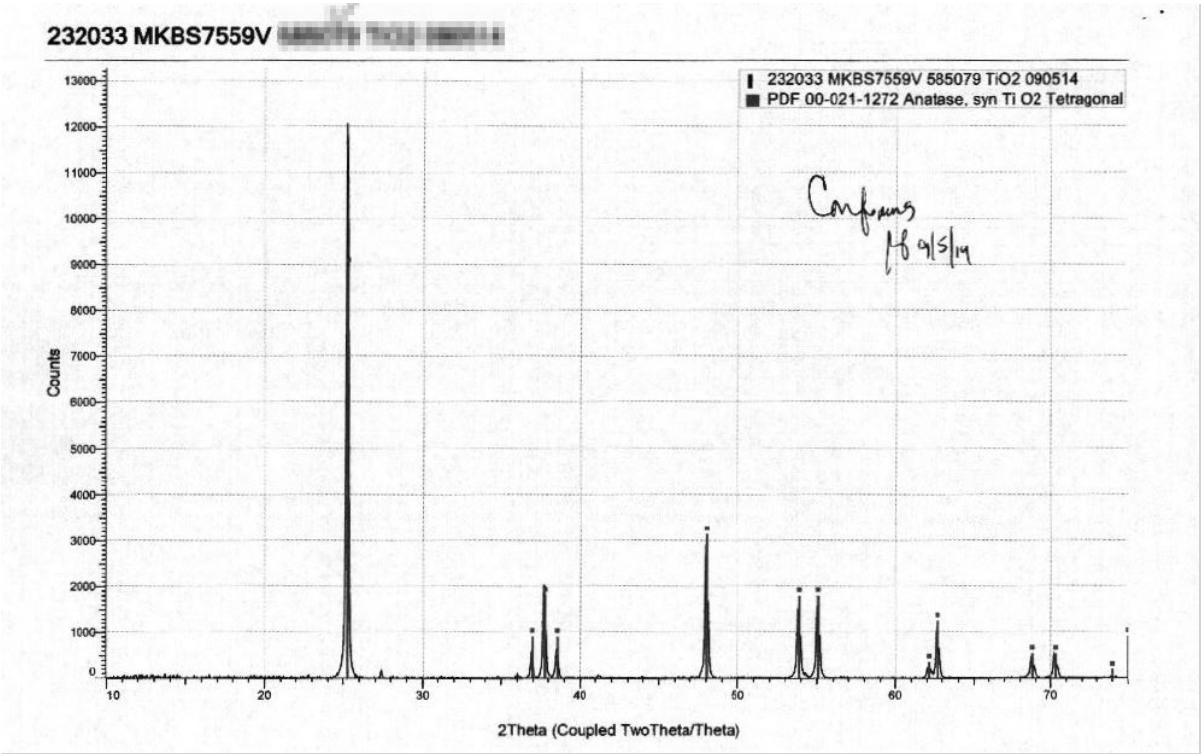

Figure S9
Pawley refinement fit for TiO_2 minerals: commercial anatase, anatase 1, anatase 2, and rutile.

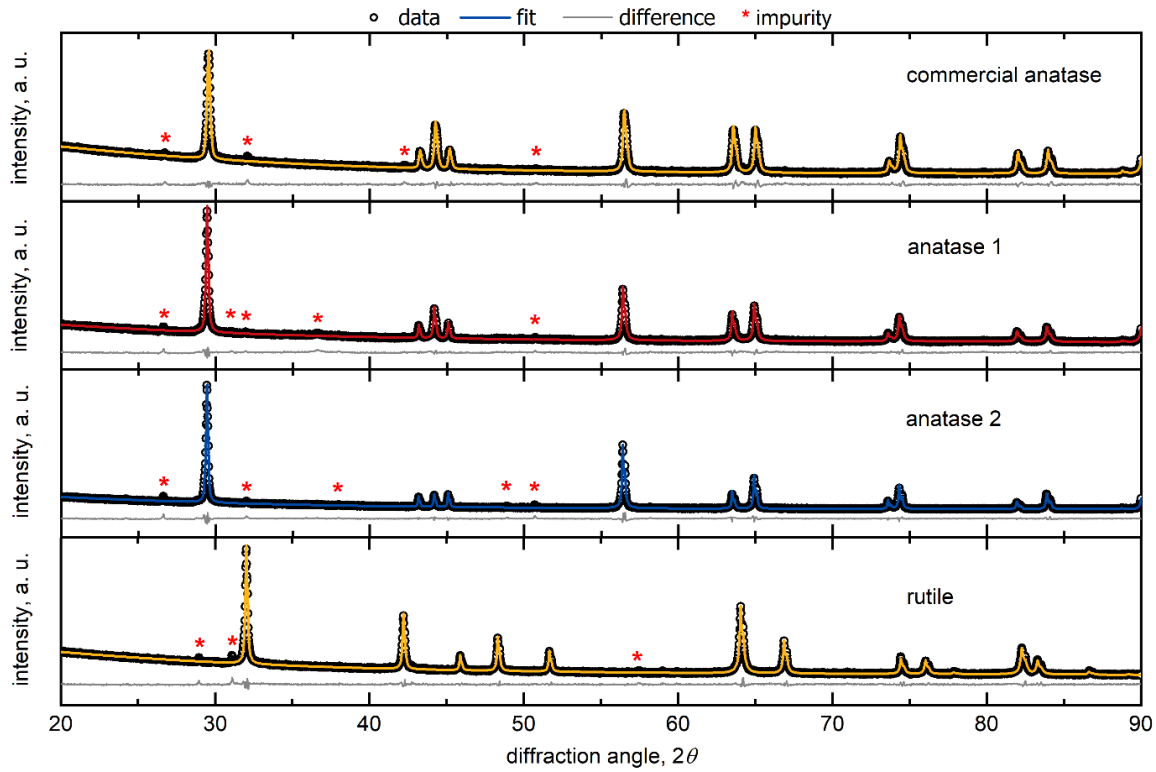

Figure S10
Pawley refinement fit for remaining minerals. Ilmenite, titanite 1, titanite 2, phlogopite, and augite are fit with only one phase, whereas the hastingsite sample has diffraction peaks from hastingsite (black ticks), magnetite (dark grey ticks), and quartz (light grey ticks), and the epidote sample has diffraction peaks from epidote (black ticks) and quartz (dark grey ticks).

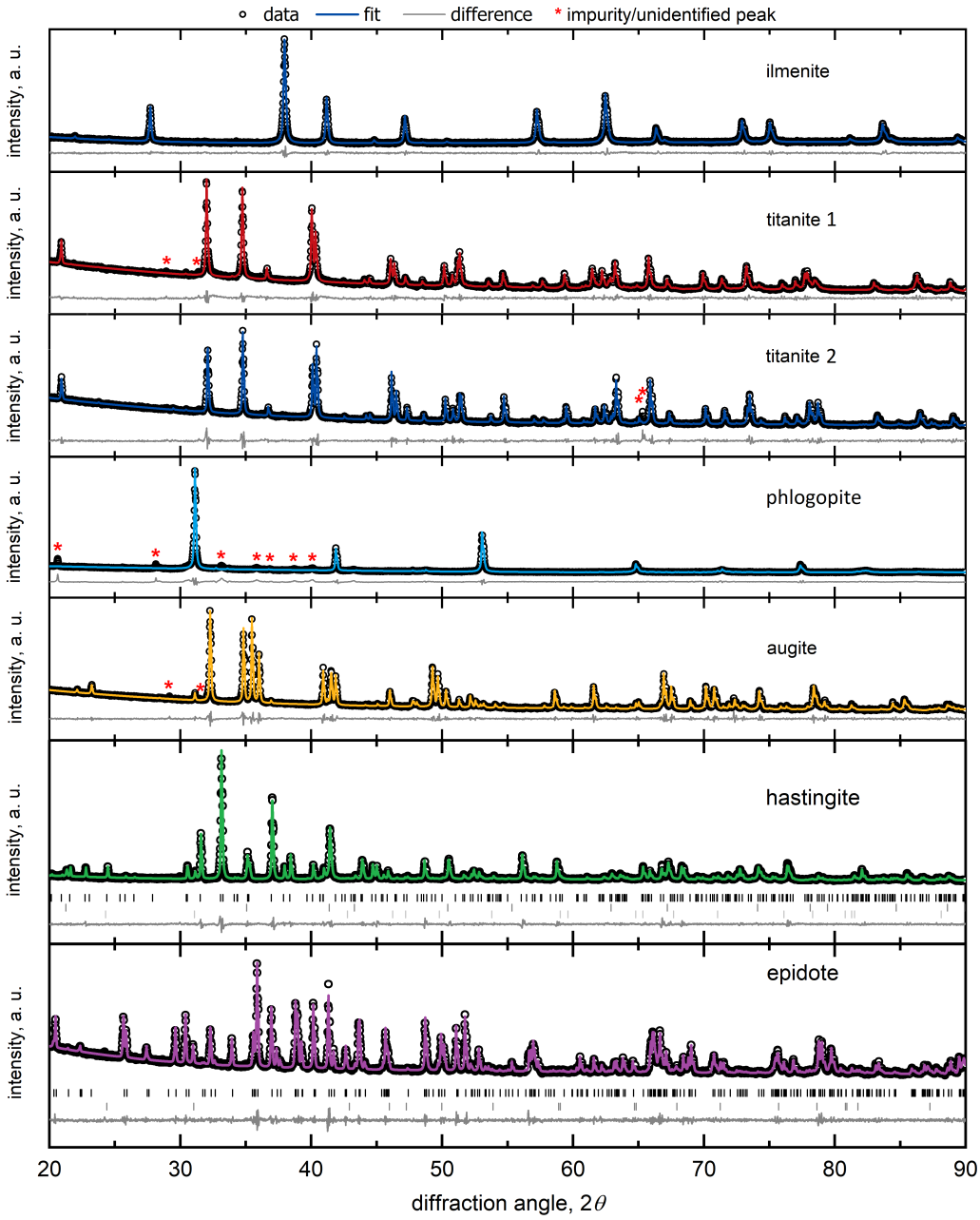

Figure S11
Kubelka–Munk plots for Ti-containing minerals, in some cases with associated band gaps: a) ilmenite, b) phlogopite, c) hastingsite, d) augite, and e) epidote.

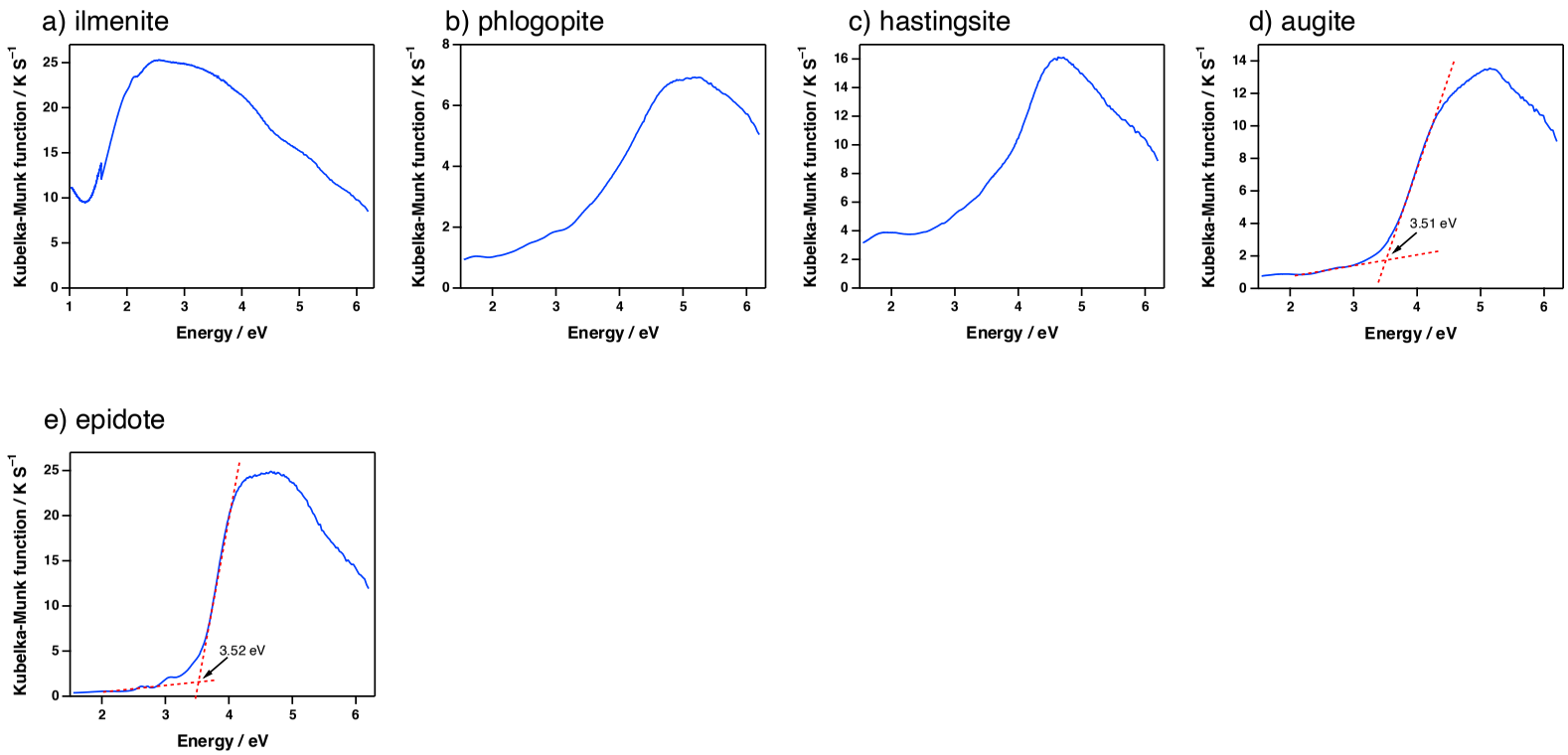

Figure S12
Secondary electron images collected by FESEM of: a) commercial anatase, b) anatase 1, c) anatase 2, d) rutile, e) titanite 1, and f) titanite 2.

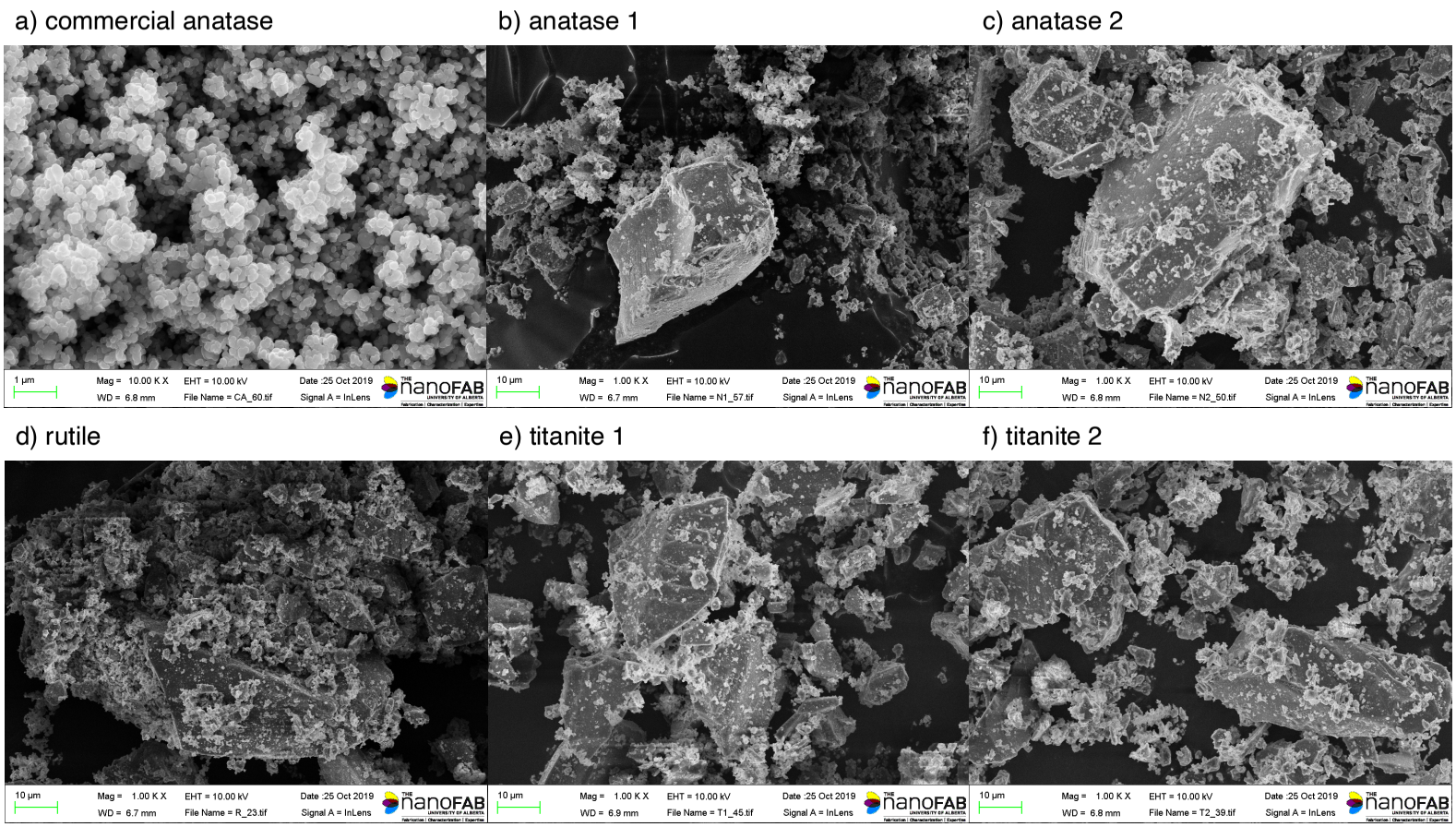

Figure S13
Influence of relative humidity on light ozone BET uptake coefficients (γ_{BET}) for TiO_2 minerals. Each data point represents 1 trial, except for RH 25%, in which each data point represents the mean of 3 trials with 1σ error bars.

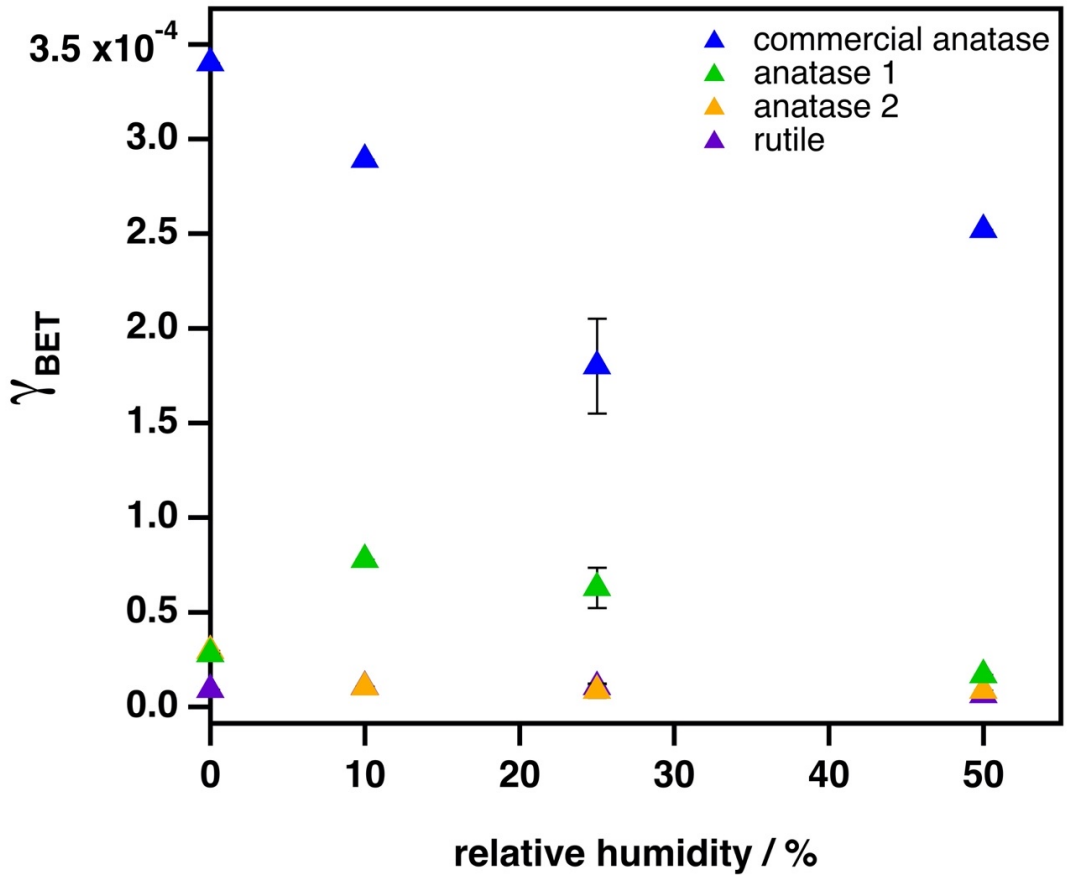

Figure S14. BET uptake coefficients (γ_{BET}) under dark and illuminated conditions for ozone at RH 25% at the surface of Ti minerals, Ti-bearing minerals, and desert dust samples (Cape Verde dust and Gobi dust). Titanite 2 dark uptake was not significantly larger than the blank experiments (as discussed in main text of the manuscript). Each data point represents the mean of 3 trials with 1σ error bars, except for ilmenite, in which each trial (n = 6) is displayed individually as this sample appeared to display bimodal reactivity (see **Section 2.1**).

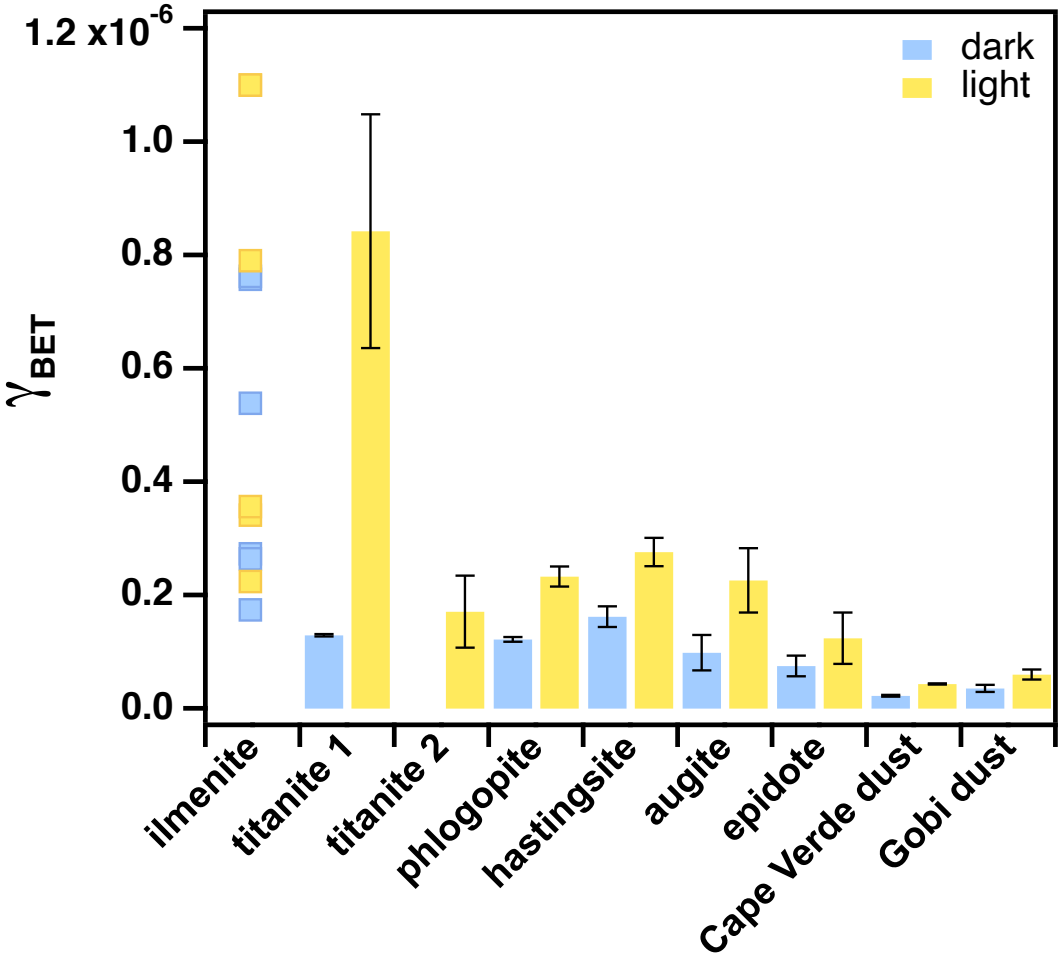

Table S1
Photochemical coated-wall flow tube parameters.

Parameter	Experimental	Equation
Temperature (T)	296.5 K	
Pressure (P)	1 atm	
Flow tube reactor diameter ($D_{reactor}$)	1.6 cm	
Flow tube reactor length ($L_{reactor}$)	34.4 cm	
Pyrex insert tube diameter (D_{tube})	1.05 cm	
Pyrex insert tube length (L_{tube})	20 cm	
Flow reactor cross-sectional area (A)	0.865 cm^2	$A = \pi r^2$
Volumetric flow (F)	0.440 L min^{-1}	
Linear velocity (v)	8.47 cm s^{-1}	$v = \frac{F}{A}$
Length of coated tube (L)	14.0 cm	
Residence time (t)	1.6 s	$t = \frac{v}{L}$
Reynolds number (Re)*	59.3	$Re = \frac{\rho \times D_{tube} \times v}{\eta}$
Length to laminar flow (l)[10]	2.18 cm	$l = 0.035 \times Re \times D_{tube}$
Mean molecular velocity (ω)**	361.6 m s^{-1}	$\omega = \sqrt{\frac{8RT}{\pi M}}$
Ozone diffusion coefficient (D)[54]	0.13 cm^2 s^{-2}	
Mean free path (λ)	105.7 nm	$\lambda = \frac{D}{\omega}$
Knudsen number (Kn)	2.00×10^{-5}	$Kn = \frac{2 \times \lambda}{D_{tube}}$
Dimensionless axial distance (z^*)[10]	0.38	$z^* = z\frac{\pi D}{2F}$

		z = axial distance of tube (L)
Effective Sherwood number (N_{Shw}^{eff})[10]	3.97	$N_{Shw}^{eff} = 3.6568 + \frac{A}{(z^* + B)}$ [55] A = 0.0978 and B = 0.0154

*Re calculations require density (ρ) and viscosity (η) of air, which are taken to be 1.2 kg m^{-3} and 1.8 x 10^{-5} Pa s, respectively at 296.5 K[55]
**ω calculations require the ideal gas constant (R) and the molar mass of ozone (M), which are 8.3145 J K^{-1} mol^{-1} and 48 x 10^{-3} kg mol^{-1}

Table S2
TiO_2/SiO_2 mixtures prepared for each TiO_2 sample.

Sample	Mass of SiO_2 (mg)	Mass of TiO_2 (mg)	TiO_2 wt. %
Commercial anatase	899.2	0.87	0.1
Anatase 1	891.0	9.00	1.0
Anatase 2	720	180.08	20.0
Rutile	809.7	90.37	10.0

Table S3
Summary of mineral sample pretreatments.

Sample	Dremel®	SUPER IRON out® (0.04 g mL^{-1})	HCl (1 M)
Anatase 1	✓		
Anatase 2			
Rutile			
Ilmenite			
Titanite 1	✓		✓
Titanite 2			
Phlogopite	✓	✓	✓
Hastingsite		✓	
Augite		✓	
Epidote	✓	✓	

Table S4
Specific surface areas (BET; $m^2\ g^{-1}$) of each mineral sample under study.

Sample	BET surface area ($m^2\ g^{-1}$)
Commercial anatase	9.6791
Anatase 1	3.7258
Anatase 2	1.5205
Rutile	1.9323
Ilmenite	2.0914
Titanite 1	1.9616
Titanite 2	1.0077
Phlogopite	18.7799
Hastingsite	1.7424
Augite	1.6235
Epidote	1.3855
Silicon dioxide	94.5500

Table S5
Elemental composition of anatase 1 as obtained via electron microprobe analysis. In all cases, results less than the estimated limit of detection are reported as zero.

	Nb_2O_5	SiO_2	TiO_2	ZnO	Al_2O_3	V_2O_3	Cr_2O_3	Fe_2O_3	MnO	MgO	CaO	Na_2O	K_2O	Total
	0.09	0.00	99.63	0.00	0.00	0.03	0.00	0.00	0.00	0.00	0.00	0.00	0.00	99.75
	0.07	0.00	100.12	0.00	0.00	0.08	0.00	0.00	0.00	0.00	0.00	0.00	0.00	100.27
	0.08	0.00	99.19	0.00	0.00	0.10	0.00	0.09	0.00	0.00	0.00	0.00	0.00	99.46
	0.07	0.00	99.70	0.00	0.00	0.00	0.00	0.00	0.00	0.00	0.00	0.00	0.00	99.77
	0.12	0.02	99.51	0.00	0.01	0.04	0.00	0.03	0.00	0.00	0.00	0.00	0.00	99.73
	0.00	0.00	99.30	0.00	0.02	0.06	0.00	0.03	0.00	0.00	0.00	0.00	0.00	99.41
	0.00	0.00	99.14	0.00	0.00	0.11	0.00	0.00	0.00	0.00	0.01	0.00	0.00	99.26
	0.10	0.00	99.14	0.00	0.00	0.10	0.00	0.05	0.00	0.00	0.00	0.00	0.00	99.39
Average	0.07	0.00	99.47	0.00	0.00	0.07	0.00	0.03	0.00	0.00	0.00	0.00	0.00	99.63
Std Dev.	0.04	0.01	0.34	0.00	0.01	0.04	0.00	0.03	0.00	0.00	0.00	0.00	0.00	0.32
Min	0.00	0.00	99.14	0.00	0.00	0.00	0.00	0.00	0.00	0.00	0.00	0.00	0.00	99.26
Max	0.12	0.02	100.12	0.00	0.02	0.11	0.00	0.09	0.00	0.00	0.01	0.00	0.00	100.27

Table S6
Elemental composition of anatase 2 as obtained via electron microprobe analysis. In all cases, results less than the estimated limit of detection are reported as zero.

	Nb_2O_5	SiO_2	TiO_2	ZnO	Al_2O_3	Cr_2O_3	Fe_2O_3	MnO	MgO	CaO	Na_2O	K_2O	Total
	0.00	0.00	100.08	0.00	0.00	0.00	0.03	0.00	0.00	0.00	0.00	0.00	100.11
	0.00	0.00	100.02	0.00	0.00	0.00	0.10	0.00	0.00	0.00	0.00	0.00	100.12
	0.00	0.00	99.89	0.03	0.00	0.00	0.09	0.00	0.00	0.00	0.00	0.00	100.01
	0.00	0.00	99.80	0.00	0.00	0.00	0.06	0.00	0.00	0.00	0.00	0.00	99.86
	0.00	0.00	99.68	0.03	0.00	0.00	0.11	0.00	0.00	0.00	0.00	0.00	99.82
	0.00	0.00	99.67	0.00	0.03	0.00	0.05	0.00	0.00	0.00	0.00	0.00	99.75
	0.00	0.00	100.20	0.00	0.00	0.00	0.05	0.00	0.00	0.00	0.00	0.00	100.25
	0.00	0.00	99.81	0.00	0.00	0.00	0.08	0.00	0.00	0.00	0.00	0.00	99.89
	0.00	0.00	99.63	0.00	0.00	0.00	0.03	0.00	0.00	0.00	0.00	0.00	99.66
	0.00	0.00	99.78	0.00	0.00	0.00	0.03	0.00	0.00	0.00	0.00	0.00	99.81
	0.04	0.00	99.81	0.00	0.00	0.00	0.06	0.00	0.00	0.00	0.00	0.00	99.91
	0.00	0.00	99.89	0.00	0.00	0.00	0.08	0.00	0.00	0.00	0.00	0.00	99.97
	0.00	0.00	99.79	0.00	0.00	0.00	0.08	0.00	0.00	0.00	0.00	0.00	99.87
	0.00	0.00	99.78	0.00	0.03	0.00	0.08	0.00	0.00	0.00	0.00	0.01	99.90
	0.00	0.00	99.72	0.00	0.00	0.00	0.07	0.00	0.00	0.00	0.00	0.00	99.79
	0.00	0.00	99.79	0.00	0.02	0.00	0.06	0.00	0.00	0.00	0.00	0.00	99.87
Average	0.00	0.00	99.83	0.00	0.01	0.00	0.07	0.00	0.00	0.00	0.00	0.00	99.91
Std Dev.	0.01	0.00	0.15	0.01	0.01	0.00	0.02	0.00	0.00	0.00	0.00	0.00	0.15
Min	0.00	0.00	99.63	0.00	0.00	0.00	0.03	0.00	0.00	0.00	0.00	0.00	99.66
Max	0.04	0.00	100.20	0.03	0.03	0.00	0.11	0.00	0.00	0.00	0.00	0.01	100.25

Table S7
Elemental composition of rutile as obtained via electron microprobe analysis. In all cases, results less than the estimated limit of detection are reported as zero.

	Nb_2O_5	SiO_2	TiO_2	ZnO	Al_2O_3	V_2O_3	Cr_2O_3	Fe_2O_3	MnO	MgO	CaO	Na_2O	K_2O	Total
	0.49	0.00	98.73	0.00	0.04	0.00	0.00	0.68	0.00	0.00	0.00	0.00	0.00	99.94
	0.50	0.00	98.74	0.00	0.04	0.05	0.00	0.67	0.00	0.00	0.00	0.00	0.00	100.00
	0.54	0.01	98.72	0.00	0.03	0.12	0.00	0.67	0.00	0.00	0.00	0.00	0.00	100.09
	0.48	0.00	98.63	0.00	0.03	0.19	0.00	0.66	0.00	0.00	0.00	0.00	0.00	99.99
	0.60	0.02	98.74	0.00	0.02	0.12	0.00	0.66	0.00	0.00	0.00	0.00	0.00	100.16
	0.52	0.00	98.93	0.00	0.03	0.14	0.00	0.68	0.00	0.00	0.00	0.00	0.00	100.30
	0.49	0.00	98.90	0.00	0.04	0.13	0.00	0.68	0.00	0.00	0.00	0.00	0.00	100.24
	0.51	0.00	98.86	0.00	0.02	0.14	0.00	0.64	0.00	0.00	0.00	0.00	0.00	100.17
Average	0.52	0.00	98.78	0.00	0.03	0.11	0.00	0.67	0.00	0.00	0.00	0.00	0.00	100.11
Std Dev.	0.04	0.01	0.10	0.00	0.01	0.06	0.00	0.01	0.00	0.00	0.00	0.00	0.00	0.13
Min	0.48	0.00	98.63	0.00	0.02	0.00	0.00	0.64	0.00	0.00	0.00	0.00	0.00	99.94
Max	0.60	0.02	98.93	0.00	0.04	0.19	0.00	0.68	0.00	0.00	0.00	0.00	0.00	100.30

Table S8
Elemental composition of ilmenite as obtained via electron microprobe analysis. In all cases, results less than the estimated limit of detection are reported as zero. We note that the impurity in the ilmenite sample was not used in the overall average for the elemental composition.

	Nb_2O_5	SiO_2	TiO_2	ZnO	Al_2O_3	V_2O_3	Cr_2O_3	FeO	MnO	MgO	CaO	Na_2O	K_2O	Total
	0.00	0.02	50.01	0.04	0.00	0.00	0.00	46.09	0.66	0.00	0.00	0.00	0.00	96.82
	0.00	0.00	50.73	0.00	0.00	0.00	0.00	46.03	0.71	0.00	0.00	0.00	0.00	97.47
	0.00	0.00	50.94	0.04	0.00	0.00	0.00	45.86	0.69	0.00	0.00	0.00	0.00	97.53
	0.00	0.01	50.10	0.03	0.00	0.00	0.00	46.43	0.69	0.00	0.00	0.00	0.00	97.26
	0.47	0.00	51.44	0.00	0.00	0.00	0.00	44.53	0.71	0.00	0.00	0.00	0.00	97.15
	0.00	0.00	50.49	0.03	0.00	0.00	0.00	45.87	0.71	0.00	0.00	0.00	0.00	97.1
	4.48	0.00	53.50	0.00	0.02	0.06	0.00	38.96	0.60	0.03	0.00	0.00	0.00	97.65
Average	0.71	0.00	51.03	0.02	0.00	0.01	0.00	44.82	0.68	0.00	0.00	0.00	0.00	97.28
Std Dev.	1.67	0.01	1.19	0.02	0.01	0.02	0.00	2.65	0.04	0.01	0.00	0.00	0.00	0.29
Min	0.00	0.00	50.01	0.00	0.00	0.00	0.00	38.96	0.60	0.00	0.00	0.00	0.00	96.82
Max	4.48	0.02	53.50	0.04	0.02	0.06	0.00	46.43	0.71	0.03	0.00	0.00	0.00	97.65
Impurity	0.00	3.47	14.82	0.00	1.53	0.04	0.00	66.95	0.39	0.14	0.00	0.00	0.00	87.42

Table S9
Elemental composition of titanite 1 as obtained via electron microprobe analysis. In all cases, results less than the estimated limit of detection are reported as zero.

	Nb_2O_5	SiO_2	TiO_2	ZnO	Al_2O_3	V_2O_3	Cr_2O_3	Fe_2O_3	MnO	MgO	CaO	Na_2O	K_2O	Total
	1.14	30.35	34.98	0.00	1.23	0.00	0.00	2.33	0.08	0.06	27.22	0.30	0.00	97.69
	1.08	30.50	34.98	0.00	1.20	0.04	0.00	2.29	0.08	0.04	27.34	0.32	0.00	97.87
	1.13	30.12	34.72	0.00	1.23	0.06	0.00	2.30	0.09	0.05	27.22	0.32	0.00	97.24
	1.16	30.23	34.86	0.00	1.19	0.04	0.00	2.31	0.09	0.08	27.08	0.29	0.00	97.33
	1.11	30.04	34.70	0.00	1.17	0.06	0.00	2.29	0.08	0.06	27.14	0.33	0.00	96.98
	0.93	30.23	34.39	0.00	1.27	0.00	0.00	2.38	0.08	0.08	27.24	0.30	0.00	96.90
	0.91	30.10	34.51	0.00	1.33	0.06	0.00	2.42	0.08	0.08	27.12	0.29	0.00	96.90
	0.98	30.32	34.59	0.00	1.29	0.00	0.00	2.40	0.08	0.07	27.26	0.29	0.00	97.28
Average	1.06	30.24	34.72	0.00	1.24	0.03	0.00	2.34	0.08	0.07	27.20	0.31	0.00	97.27
Std Dev.	0.10	0.15	0.22	0.00	0.05	0.03	0.00	0.05	0.00	0.02	0.08	0.02	0.00	0.36
Min	0.91	30.04	34.39	0.00	1.17	0.00	0.00	2.29	0.08	0.04	27.08	0.29	0.00	96.90
Max	1.16	30.50	34.98	0.00	1.33	0.06	0.00	2.42	0.09	0.08	27.34	0.33	0.00	97.87

Table S10
Elemental composition of titanite 2 as obtained via electron microprobe analysis. In all cases, results less than the estimated limit of detection are reported as zero.

	Nb_2O_5	SiO_2	TiO_2	ZnO	Al_2O_3	Cr_2O_3	Fe_2O_3	MnO	MgO	CaO	Na_2O	K_2O	Total
	0.00	30.81	38.44	0.00	0.86	0.00	0.57	0.00	0.03	28.25	0.00	0.00	98.96
	0.00	30.78	38.68	0.00	0.82	0.00	0.53	0.00	0.03	28.22	0.00	0.00	99.06
	0.00	30.72	38.16	0.00	0.86	0.00	0.57	0.00	0.04	28.30	0.12	0.00	98.77
	0.00	30.78	38.17	0.00	0.86	0.00	0.57	0.00	0.02	28.30	0.00	0.00	98.70
	0.00	30.74	38.26	0.00	0.90	0.00	0.57	0.00	0.02	28.33	0.00	0.00	98.82
	0.00	30.76	38.33	0.00	0.88	0.00	0.57	0.03	0.03	28.35	0.00	0.00	98.95
	0.00	30.75	38.42	0.00	0.96	0.00	0.62	0.00	0.02	28.31	0.00	0.00	99.08
	0.00	30.75	38.64	0.00	0.83	0.00	0.52	0.00	0.03	28.42	0.00	0.00	99.19
	0.00	30.70	38.76	0.00	0.71	0.00	0.50	0.02	0.04	28.26	0.00	0.00	98.99
	0.00	30.77	38.46	0.00	0.90	0.00	0.57	0.02	0.03	28.29	0.00	0.00	99.04
	0.00	30.77	38.31	0.00	0.88	0.00	0.58	0.02	0.03	28.28	0.03	0.00	98.90
	0.00	30.85	38.44	0.00	0.90	0.00	0.58	0.00	0.02	28.39	0.00	0.00	99.18
	0.00	30.76	38.51	0.00	0.85	0.00	0.61	0.00	0.03	28.27	0.00	0.00	99.03
	0.00	30.78	38.51	0.00	0.87	0.00	0.58	0.00	0.03	28.37	0.00	0.00	99.14
	0.00	30.79	38.64	0.00	0.86	0.00	0.59	0.02	0.02	28.29	0.00	0.00	99.21
	0.00	30.73	38.83	0.00	0.70	0.00	0.49	0.00	0.02	28.38	0.00	0.00	99.15
Average	0.00	30.77	38.47	0.00	0.85	0.00	0.56	0.01	0.03	28.31	0.01	0.00	99.01
Std Dev.	0.00	0.04	0.20	0.00	0.07	0.00	0.04	0.01	0.01	0.06	0.03	0.00	0.15
Min	0.00	30.70	38.16	0.00	0.70	0.00	0.49	0.00	0.02	28.22	0.00	0.00	98.70
Max	0.00	30.85	38.83	0.00	0.96	0.00	0.62	0.03	0.04	28.42	0.12	0.00	99.21

Table S11
Elemental composition of phlogopite as obtained via electron microprobe analysis. In all cases, results less than the estimated limit of detection are reported as zero.

	Nb_2O_5	SiO_2	TiO_2	ZnO	Al_2O_3	V_2O_3	Cr_2O_3	FeO	MnO	MgO	CaO	Na_2O	K_2O	Total
	0.00	42.82	0.92	0.08	11.08	0.00	0.00	6.66	0.13	22.43	0.00	0.43	10.07	94.62
	0.00	42.80	0.98	0.08	11.02	0.00	0.00	6.60	0.13	22.23	0.00	0.18	10.51	94.53
	0.00	42.85	1.05	0.07	11.20	0.00	0.00	6.80	0.13	22.05	0.00	0.25	10.31	94.71
	0.00	42.53	1.02	0.09	11.19	0.00	0.00	6.79	0.12	22.26	0.00	0.34	10.17	94.51
	0.00	42.83	1.04	0.07	11.10	0.00	0.00	6.68	0.12	22.13	0.00	0.25	10.39	94.61
	0.00	42.68	1.05	0.08	10.95	0.00	0.00	6.79	0.12	22.05	0.00	0.33	10.25	94.30
	0.00	42.23	1.07	0.06	11.17	0.00	0.00	6.88	0.14	22.15	0.00	0.36	10.17	94.23
Average	0.00	42.68	1.02	0.08	11.10	0.00	0.00	6.74	0.13	22.19	0.00	0.31	10.27	94.50
Std Dev.	0.00	0.23	0.05	0.01	0.09	0.00	0.00	0.10	0.01	0.13	0.00	0.08	0.15	0.18
Min	0.00	42.23	0.92	0.06	10.95	0.00	0.00	6.60	0.12	22.05	0.00	0.18	10.07	94.23
Max	0.00	42.85	1.07	0.09	11.20	0.00	0.00	6.88	0.14	22.43	0.00	0.43	10.51	94.71

Table S12
Elemental composition of hastingsite as obtained via electron microprobe analysis. In all cases, results less than the estimated limit of detection are reported as zero.

	Nb_2O_5	SiO_2	TiO_2	ZnO	Al_2O_3	V_2O_3	Cr_2O_3	FeO	MnO	MgO	CaO	Na_2O	K_2O	Total
	0.00	40.95	0.80	0.00	10.59	0.00	0.00	21.01	0.21	8.76	11.17	1.68	2.07	97.24
	0.00	40.79	0.77	0.00	10.58	0.00	0.00	20.96	0.23	8.66	11.14	1.63	2.02	96.78
	0.00	40.86	0.76	0.03	10.42	0.00	0.00	20.96	0.20	8.64	11.16	1.63	2.02	96.68
	0.00	40.72	0.78	0.03	10.43	0.00	0.00	20.98	0.20	8.59	11.08	1.63	2.02	96.46
	0.00	40.58	0.76	0.00	10.53	0.00	0.00	21.02	0.21	8.73	11.14	1.67	2.02	96.66
	0.00	40.63	0.84	0.03	10.46	0.00	0.00	20.91	0.20	8.62	11.12	1.64	2.07	96.52
	0.00	40.75	0.76	0.00	10.37	0.00	0.00	21.00	0.19	8.66	11.11	1.69	2.03	96.56
	0.00	40.79	0.81	0.00	10.44	0.00	0.00	21.00	0.22	8.68	11.11	1.64	2.02	96.71
Average	0.00	40.76	0.79	0.01	10.48	0.00	0.00	20.98	0.21	8.67	11.13	1.65	2.03	96.70
Std Dev.	0.00	0.12	0.03	0.02	0.08	0.00	0.00	0.04	0.01	0.06	0.03	0.02	0.02	0.24
Min	0.00	40.58	0.76	0.00	10.37	0.00	0.00	20.91	0.19	8.59	11.08	1.63	2.02	96.46
Max	0.00	40.95	0.84	0.03	10.59	0.00	0.00	21.02	0.23	8.76	11.17	1.69	2.07	97.24

Table S13
Elemental composition of augite as obtained via electron microprobe analysis. In all cases, results less than the estimated limit of detection are reported as zero.

	Nb_2O_5	SiO_2	TiO_2	ZnO	Al_2O_3	V_2O_3	Cr_2O_3	FeO	MnO	MgO	CaO	Na_2O	K_2O	Total
	0.00	50.90	0.76	0.00	3.39	0.00	0.58	5.81	0.11	16.41	19.70	0.33	0.00	97.99
	0.00	51.55	0.64	0.00	2.88	0.00	0.55	5.69	0.13	16.94	19.57	0.34	0.00	98.29
	0.00	51.96	0.55	0.00	2.49	0.00	0.67	5.41	0.11	17.32	19.72	0.32	0.00	98.55
	0.00	51.55	0.73	0.00	2.98	0.03	0.69	5.45	0.12	16.51	20.15	0.33	0.00	98.54
	0.00	51.31	0.77	0.00	3.09	0.06	0.60	5.54	0.12	16.56	20.19	0.37	0.00	98.61
	0.00	51.46	0.76	0.00	3.18	0.00	0.61	5.61	0.13	16.61	20.12	0.35	0.00	98.83
	0.00	51.74	0.75	0.00	3.38	0.03	0.61	5.70	0.11	16.68	20.20	0.33	0.00	99.53
	0.00	52.26	0.75	0.00	3.41	0.00	0.59	5.80	0.13	16.80	20.25	0.37	0.00	100.36
Average	0.00	51.59	0.71	0.00	3.10	0.02	0.61	5.63	0.12	16.73	19.99	0.34	0.00	98.84
Std Dev.	0.00	0.41	0.08	0.00	0.32	0.02	0.05	0.15	0.01	0.29	0.27	0.02	0.00	0.76
Min	0.00	50.90	0.55	0.00	2.49	0.00	0.55	5.41	0.11	16.41	19.57	0.32	0.00	97.99
Max	0.00	52.26	0.77	0.00	3.41	0.06	0.69	5.81	0.13	17.32	20.25	0.37	0.00	100.36

Table S14
Elemental composition of epidote as obtained via electron microprobe analysis. In all cases, results less than the estimated limit of detection are reported as zero.

	Nb_2O_5	SiO_2	TiO_2	ZnO	Al_2O_3	V_2O_3	Cr_2O_3	Fe_2O_3	MnO	MgO	CaO	Na_2O	K_2O	Total
	0.00	37.19	0.22	0.00	22.39	0.05	0.00	14.18	0.14	0.03	23.03	0.00	0.00	97.23
	0.00	37.03	0.23	0.00	22.62	0.04	0.00	14.13	0.14	0.03	23.16	0.00	0.00	97.38
	0.00	37.31	0.17	0.00	22.66	0.05	0.00	14.24	0.14	0.03	23.01	0.00	0.00	97.61
	0.00	37.02	0.23	0.00	22.60	0.04	0.00	14.15	0.13	0.04	23.02	0.00	0.00	97.23
	0.00	37.20	0.20	0.00	22.63	0.05	0.00	14.18	0.12	0.03	23.03	0.00	0.00	97.44
	0.00	37.13	0.20	0.00	22.49	0.04	0.00	14.18	0.11	0.05	23.07	0.00	0.00	97.27
	0.00	37.20	0.20	0.00	22.53	0.04	0.00	14.23	0.12	0.03	23.13	0.00	0.00	97.48
	0.00	37.19	0.22	0.00	22.38	0.05	0.00	14.34	0.12	0.02	23.13	0.00	0.00	97.45
Average	0.00	37.16	0.21	0.00	22.54	0.05	0.00	14.20	0.13	0.03	23.07	0.00	0.00	97.39
Std Dev.	0.00	0.10	0.02	0.00	0.11	0.01	0.00	0.07	0.01	0.01	0.06	0.00	0.00	0.14
Min	0.00	37.02	0.17	0.00	22.38	0.04	0.00	14.13	0.11	0.02	23.01	0.00	0.00	97.23
Max	0.00	37.31	0.23	0.00	22.66	0.05	0.00	14.34	0.14	0.05	23.16	0.00	0.00	97.61

Table S15. Crystallographic data for Ti-containing sample refinement.

sample	Commercial anatase	Anatase 1	Anatase 2	Rutile
space group	$I4_1/amd$ (No. 136)	$I4_1/amd$ (No. 136)	$I4_1/amd$ (No. 136)	$P4_2/mnm$ (No. 136)
a (Å)	3.78645(5)	3.78514(4)	3.78489(3)	4.59572(6)
b(Å)	3.78645(5)	3.78514(4)	3.78489(3)	4.59572(6)
c (Å)	9.5179(1)	9.5120(1)	9.5119(1)	2.95966(4)
α,°	90	90	90	90
β,°	90	90	90	90
γ,°	90	90	90	90
T (K)	296	296	296	296
radiation	Co Kα,	Co Kα,	Co Kα,	Co Kα,
	Kα1 λ=1.78900 Å	Kα1 λ=1.78900 Å	Kα1 λ=1.78900 Å	Kα1 λ=1.78900 Å
	Kα2 λ=1.79283 Å	Kα2 λ=1.79283 Å	Kα2 λ=1.79283 Å	Kα2 λ=1.79283 Å
2θ limits	20.00–90.00°	20.00–90.00°	20.00–90.00°	20.00–90.00°
refinement method	Pawley	Pawley	Pawley	Pawley
no. of data collected	3500 data points	3500 data points	3500 data points	3500 data points
no. of Bragg reflections	14	14	14	13
no. of variables	27	27	27	27
residuals	R_{wp} = 0.0472	R_{wp} = 0.0492	R_{wp} = 0.0657	R_{wp} = 0.0482

$$R_{wp} = \left[\sum\left[w(y_o - y_c)\right] / \sum w y_o^2\right]^{1/2}$$

sample	Titanite 1	Titanite 2	Phlogopite	Augite	Hastingsite	Epidote	ilmenite
space group	$C2/c$ (No. 15)	$C2/c$ (No. 15)	$C2/m$ (No. 12)	$C2/c$ (No. 15)	$C2/m$ (No. 12)	$P2_1/m$ (No. 11)	$R\bar{3}$ (No. 148)
a (Å)	6.5529(1)	6.5735(1)	5.1635(2)	9.7361(2)	9.9076(1)	8.8986(1)	5.08769(7)
b(Å)	8.7022(2)	8.7278(1)	9.0833(6)	8.8989(1)	18.1624(4)	5.63531(8)	5.08769(7)
c (Å)	7.0569(1)	7.0851(1)	20.086(2)	5.2686(1)	5.3283(3)	10.1623(1)	4.0820(2)
α,°	90	90	90	90	90	90	90
β,°	113.849(1)	113.962(1)	95.685(3)	106.327(1)	104.992(3)	115.4145(8)	90
γ,°	90	90	90	90	90	90	120
T (K)	296	296	296	296	296	296	296
radiation	Co Kα,	Co Kα,	Co Kα,	Co Kα,	Co Kα,	Co Kα,	Co Kα,
	Kα1 λ=1.78900 Å	Kα1 λ=1.78900 Å	Kα1 λ=1.78900 Å	Kα1 λ=1.78900 Å	Kα1 λ=1.78900 Å	Kα1 λ=1.78900 Å	Kα1 λ=1.78900 Å
	Kα2 λ=1.79283 Å	Kα2 λ=1.79283 Å	Kα2 λ=1.79283 Å	Kα2 λ=1.79283 Å	Kα2 λ=1.79283 Å	Kα2 λ=1.79283 Å	Kα2 λ=1.79283 Å
2θ limits	20.00–90.00°	20.00–90.00°	20.00–90.00°	20.00–90.00°	20.00–90.00°	20.00–90.00°	20.00–90.00°
refinement method	Pawley	Pawley	Pawley	Pawley	Pawley	Pawley	Pawley
no. of data collected	3500 data points	3500 data points	3500 data points	3500 data points	3500 data points	3500 data points	3500 data points
no. of Bragg reflections	189	189	257	14	258	281	36
no. of variables	205	205	273	27	330	333	50
residuals	R_{wp} = 0.0731	R_{wp} = 0.0482	R_{wp} = 0.0923	R_{wp} = 0.0526	R_{wp} = 0.0347	R_{wp} = 0.0358	R_{wp} = 0.0201

$$R_{wp} = \left[\sum\left[w(y_o - y_c)\right] / \sum w y_o^2\right]^{1/2}$$

Table S16. Crystallographic data for anatase 2 and titanite 1 single crystals

Formula	**TiO_2**	**$CaTiSiO_5$**
Formula mass (amu)	79.90	196.07
Space group	$I4_1/amd$ (No. 136)	$C2/c$ (No. 15)
a (Å)	3.806(4)	6.572(3)
b (Å)	3.806(4)	8.731(3)
c (Å)	9.576(9)	7.084(4)
α, °	90	90
β, °	90	113.922(4)
γ, °	90	90
V (Å^3)	138.7(2)	371.6(3)
Z	4	4
ρ_{calcd} (g cm^{-3})	3.825	3.505
T (K)	296(2)	296(2)
Crystal dimensions (mm)	0.01 × 0.08 × 0.20	0.05 × 0.12 × 0.14
Radiation	Graphite monochromated Mo $K\alpha$, λ = 0.71073 Å	
μ (Mo $K\alpha$) (mm^{-1})	5.55	3.900
Transmission factors	0.3958– 0.9313	0.6191–0.8441
2θ limits	11.54 – 95.74 °	8.24 – 66.44 °
Data collected	$-5 \le h \le 5$, $-5 \le k \le 5$, $-14 \le l \le 14$	$-9 \le h \le 10$, $-13 \le k \le 13$, $-10 \le l \le 10$
No. of data collected	917	2164
No. of unique data, including $F_o^2 < 0$	84 (R_{int} = 0.0370)	706 (R_{int} = 0.0285)
No. of unique data, with $F_o^2 > 2\sigma(F_o^2)$	72	560
No. of variables	8	41
$R(F)$ for $F_o^2 > 2\sigma(F_o^2)$ [a]	0.0127	0.0373
$R_w(F_o^2)$ [b]	0.0144	0.0481
Goodness of fit	1.231	1.084
$(\Delta\rho)_{max}$, $(\Delta\rho)_{min}$ (e Å^{-3})	0.362, – 0.448	0.644, – 1.262

[a] $R(F) = \sum||F_o| - |F_c|| / \sum|F_o|$. [b] $R_w(F_o^2) = [\sum[w(F_o^2 - F_c^2)^2] / \sum wF_o^4]^{1/2}$; $w^{-1} = [\sigma^2(F_o^2) + (Ap)^2 + Bp]$, where $p = [\max(F_o^2,0) + 2F_c^2] / 3$.

Table S17. Atomic coordinates and displacement parameters for anatase 2.

Position	Wyckoff position	x	y	z	U_{11} (Å^2)	U_{22} (Å^2)	U_{33} (Å^2)
Ti	4*b*	0	1/4	3/8	0.0081(3)	0.0081(3)	0.0059(3)
O	8*e*	0	1/4	0.1668(2)	0.0069(6)	0.0134(6)	0.0064(6)

Table S18. Selected interatomic distances (Å) for anatase 2.

Ti – O (×4)	1.945(2)
Ti – O (×2)	1.993(2)
Ti –Ti (×4)	3.058(2)

Table S19. Atomic coordinates and displacement parameters for titanite 1.

Position	Wyckoff position	x	y	z	U_{11} (Å^2)	U_{22} (Å^2)	U_{33} (Å^2)
Ti	4*a*	0	0	0	0.0102(3)	0.0118(3)	0.0225(4)
Si	4*e*	0	0.68280(9)	1/4	0.0090(4)	0.0091(4)	0.0111(4)
Ca	4*e*	0	0.33202(7)	1/4	0.0120(3)	0.0103(3)	0.0361(5)
O1	4*e*	0	0.0721(3)	1/4	0.0174(10)	0.0122(9)	0.0123(10)
O2	8*f*	0.3976(2)	0.28987(16)	0.3819(2)	0.0144(7)	0.0121(7)	0.0183(8)
O3	8*f*	0.3141(2)	0.06639(19)	0.0897(2)	0.0141(7)	0.0147(8)	0.0177(8)

Table S20. Selected interatomic distances (Å) for titanite 1.

Ti – O1 (×2)	1.879(1)
Ti – O3 (×2)	1.984(2)
Ti – O2 (×2)	2.016(2)
Si – O3 (×2)	1.640(2)
Si – O2 (×2)	1.646(2)
Ca – O1	2.269(3)
Ca – O3 (×2)	2.417(2)
Ca – O2 (×2)	2.420(2)